

Scalable quantum photonic devices emitting indistinguishable photons in the telecom C-band

Paweł Holewa,^{1,2,3, a)} Emilia Zięba-Ostój,¹ Daniel A. Vajner,⁴ Maja Wasiluk,¹ Benedek Gaál,² Aurimas Sakanas,² Marek Burakowski,¹ Paweł Mrowiński,¹ Bartosz Krajnik,¹ Meng Xiong,^{2,3} Alexander Huck,⁵ Kresten Yvind,^{2,3} Niels Gregersen,² Anna Musiał,¹ Tobias Heindel,⁴ Marcin Syperek,^{1, b)} and Elizaveta Semenova^{2,3, c)}

¹⁾*Department of Experimental Physics, Faculty of Fundamental Problems of Technology, Wrocław University of Science and Technology, Wyb. Wyspiańskiego 27, 50-370 Wrocław, Poland*

²⁾*DTU Electro, Department of Electrical and Photonics Engineering, Technical University of Denmark, Kongens Lyngby 2800, Denmark*

³⁾*NanoPhoton-Center for Nanophotonics, Technical University of Denmark, 2800 Kongens Lyngby, Denmark*

⁴⁾*Institute of Solid State Physics, Technische Universität Berlin, 10623 Berlin, Germany*

⁵⁾*Center for Macroscopic Quantum States (bigQ), Department of Physics, Technical University of Denmark, 2800 Kongens Lyngby, Denmark*

Epitaxial semiconductor quantum dots (QDs) are a promising resource for quantum light generation and the realization of non-linear quantum photonic elements operating at the single-photon level. Their random spatial distribution resulting from their self-organized nature, however, restrains the fabrication yield of quantum devices with the desired functionality. As a solution, the QDs can be imaged and localized, enabling a deterministic device fabrication. Due to the significant electronic noise of camera sensors operating in the telecommunication C-band, 1530-1560 nm, this technique remained challenging. In this work, we report on the imaging of QDs epitaxially grown on InP with emission wavelengths in the telecom C-band demonstrating a localization accuracy of 80 nm. This is enabled by the hybrid integration of QDs in a planar sample geometry with a bottom metallic reflector to enhance the out-of-plane emission. To exemplify our approach, we successfully fabricate circular Bragg grating cavities around single pre-selected QDs with an overall cavity placement uncertainty of 90 nm. QD-cavity coupling is demonstrated by a Purcell enhancement up to ~ 5 with an estimated photon extraction efficiency of $(16.6 \pm 2.7) \%$ into a numerical aperture of 0.4. We demonstrate triggered single-photon emission with $g^{(2)}(0) = (3.2 \pm 0.6) \times 10^{-3}$ and record-high photon indistinguishability associated with two-photon interference visibilities of $V = (19.3 \pm 2.6) \%$ and $V_{PS} = 99.8^{+0.2}_{-2.6} \%$ without and with temporal postselection, respectively. While the performance of our devices readily enables proof-of-principle experiments in quantum information, further improvements in the yield and coherence may enable the realization of non-linear devices at the single photon level and advanced quantum networks at the telecom wavelength.

Keywords: semiconductor quantum dots, circular Bragg gratings, InAs/InP, deterministic fabrication, telecom spectral range, single-photon sources;

INTRODUCTION

A quantum network¹ based on remote nodes interconnected via fiber-optical links and capable of transferring quantum information using flying qubits will provide the backbone for the implementation of protocols for secure communication^{2,3} and distributed quantum computing⁴. Notably, the network can rely on the existing silica-fiber-based infrastructure, utilizing a low-loss channel for the transmission of photons with a wavelength in the telecom C-band around 1550 nm⁵. These quantum network architectures can benefit from existing components and classical signal management protocols, hence making it feasible to transfer quantum information over large distances⁵.

In recent years, the technology for the epitaxial growth of self-assembled quantum dots (QDs) has rapidly advanced, resulting in the demonstration of QD-based single-photon sources (SPSs) with outstanding characteristics. These include

high photon extraction efficiencies ($\sim 79 \%$)⁶, high single photon generation rates ($\sim 1 \text{ GHz}$)⁷, and near unity photon indistinguishability ($> 96 \%$)^{7,8}, however, all achieved outside the telecom-relevant C-band. Besides the extraordinary material quality, these characteristics are achieved owing to efficient light-matter coupling between a QD and a suitable photonic element. For efficient coupling, spectral and spatial matching is required between the quantum emitter and the engineered photonic mode, which is challenging due to the spatial and spectral distribution of epitaxial QDs. Until now, the QD coupling to photonic cavities operating around 1550 nm has only been realized using non-deterministic fabrication processes, limiting device yield and scalability⁹.

In this article, we report on the scalable fabrication of nanophotonic elements around pre-selected individual QDs emitting single and indistinguishable photons in the telecom C-band. For this purpose, we developed a near-infrared (NIR) imaging technique for self-assembled InAs/InP QDs utilizing a hybrid sample geometry with enhanced out-of-plane emission from single QDs¹⁰ and a thermo-electrically cooled InGaAs camera in a wide-field imaging configuration. In combination with two electron-beam lithography (EBL) steps, our method

^{a)}Electronic mail: pawel.holewa@pwr.edu.pl

^{b)}Electronic mail: marcin.syperek@pwr.edu.pl

^{c)}Electronic mail: esem@fotonik.dtu.dk

enables an overall positioning accuracy of 90 nm of the QD with respect to the photonic element and allows for rapid data collection as compared to competing techniques based on scanning *in-situ* imaging¹¹.

We applied our technique for the deterministic integration of pre-selected QDs into circular Bragg grating (CBG) cavities. The proposed technological workflow allows us to greatly enhance the device fabrication yield reaching $\sim 30\%$, which is a significant improvement compared to $< 1\%$ that would typically be achieved with a random placement approach. The QD-CBG coupling is evidenced by a Purcell factor ~ 5 , and our devices demonstrate a state-of-the-art photon extraction efficiency of $\eta = (16.6 \pm 2.7)\%$ into the first lens with a numerical aperture (NA) of 0.4, a high single-photon purity associated with $g^{(2)}(0) = (3.2 \pm 0.6) \times 10^{-3}$, and a record-high photon-indistinguishability of $V = (19.3 \pm 2.6)\%$ for QD-based SPSS at C-band wavelengths.

RESULTS

Design of a QD structure for wide-field imaging

Imaging at extremely low light levels at wavelengths $> 1 \mu\text{m}$ is challenging due to the high level of electronic noise of respective camera systems. Although cameras based on InGaAs achieve quantum efficiencies $> 80\%$, they are characterized by a factor of $> 10^4$ higher dark currents compared to Si-based devices. The photon emission rate from the sample is therefore of key importance for the ability to image and localize single QDs. Following our previous work¹⁰, we have designed a planar sample geometry that significantly enhances the photon extraction efficiency, allowing to localize single QDs and the subsequent fabrication of photonic elements.

The planar QD structure consists of an epitaxially grown 312 nm-thick InP slab containing a single layer of InAs QDs. The InP slab is atop a 359 nm-thick SiO_2 layer with a bottom Al mirror bonded to a Si wafer carrier (Fig. 1a, see **Methods**)¹⁰. Overall, this geometry enhances the QD emission in the out-of-plane direction by a factor > 7 as compared to bulk InP samples, reaching a total photon extraction efficiency of $> 10\%$ from a single QD for NA = 0.4. For QD localization later in the experiment, we structure the top InP layer in a mesh with fields of size $(50 \times 50) \mu\text{m}^2$ separated by $10 \mu\text{m}$ -wide ridges (see **Methods**), where the field edges are used as alignment marks (AMs) for imaging. The fields are furthermore organized in blocks accompanied by InP crosses that allow us to align the electron beam to specific target QDs during the EBL process (see **Supplemental Material** for the optical microscope image of the sample surface with fabricated cavities).

For the self-assembled Stranski-Krastanov QD epitaxy, we employed the near-critical growth regime in metalorganic vapor-phase epitaxy (MOVPE)¹² (see **Supplemental Material**) and obtained a QD surface density of $3.1 \times 10^8/\text{cm}^2$ corresponding to an average QD separation of $1.5 \mu\text{m}$. Since QDs exhibit a size, shape, and strain distribution, only a fraction of the QDs have their ground-state optical transition in the C-band. With a $(1550 \pm 8) \text{ nm}$ bandpass filter, we find on av-

erage $N_F = 10$ QDs per field, which translates to an effective QD density of $4 \times 10^5/\text{cm}^2$ and an average QD separation of $\sim 16 \mu\text{m}$.

Design of circular Bragg grating cavities

The CBG geometry is optimized using the modal method (see **Supplemental Material**) to enhance the cavity figures of merit at 1550 nm, namely the collection efficiency at the first lens and the Purcell factor (F_P). As opposed to other implementations⁹, we consider a simplified CBG geometry consisting of a central mesa and only four external rings. According to our calculations, this number is sufficient for high η and F_P , providing a smaller footprint and less complexity in the fabrication process. The in-plane cavity dimensions include the central mesa radius of $R_0 = 648 \text{ nm}$, the grating period of 747 nm, and the separation between InP rings (air gap) of 346 nm. For these geometrical parameters, Fig. 1b shows the calculated broadband η that amounts to nearly 62 % and 82 % at 1550 nm for a NA of 0.4 and 0.65, respectively, which is similar to other state-of-the-art CBG designs^{13–15}. The wavelength dependence of the Purcell factor, presented in Fig. 1b, mimics the CBG cavity mode centered at 1550 nm and reaches a maximum value $F_P = 18.1$ with a quality factor of 110. The influence of the cavity geometry on the dispersion of η and F_P suggests that the cavity grating together with the Al mirror creates a photonic bandgap that governs the η -dependence and enhances the emission directionality, while the InP membrane thickness and central mesa diameter crucially affect the center wavelength of the F_P -dependence. A scanning electron microscopy (SEM) image of a fabricated CBG cavity is shown in Fig. 1c.

Optical imaging and QD localization

The NIR imaging setup utilizes a wide-field bright microscope configuration as shown in Fig. 2a. The structure with QDs above the Al reflector is mounted in an optical cryostat at $T = 4.2 \text{ K}$ movable by a x - y - z stage for targeting fabricated fields that are imaged consecutively. For sample illumination, we use a 660 nm continuous-wave semiconductor laser diode, spatially shaped with a beam expander, and focused on the backside of a commercially-available microscope objective (NA = 0.65) with $50\times$ magnification, 57 % transmission in the NIR, and 10 mm working distance. This configuration provides nearly homogeneous surface illumination across a $(50 \times 50) \mu\text{m}^2$ field and high photon collection efficiency. The spatially-distributed QD microphotoluminescence (μPL) and scattered light from the field edges (here used as AMs) are collected by the same objective and pass through a cold mirror cutting off the laser light. Finally, the emission is projected onto a thermo-electrically cooled InGaAs-based camera with a $(12.8 \times 10.24) \text{ mm}^2$ chip and a pixel size of $(20 \times 20) \mu\text{m}^2$. With the $4\times$ magnification lens in front of the camera, the setup has a $200\times$ magnification, enabling the optimal filling of the entire camera chip with a single field (Fig. 2b). The

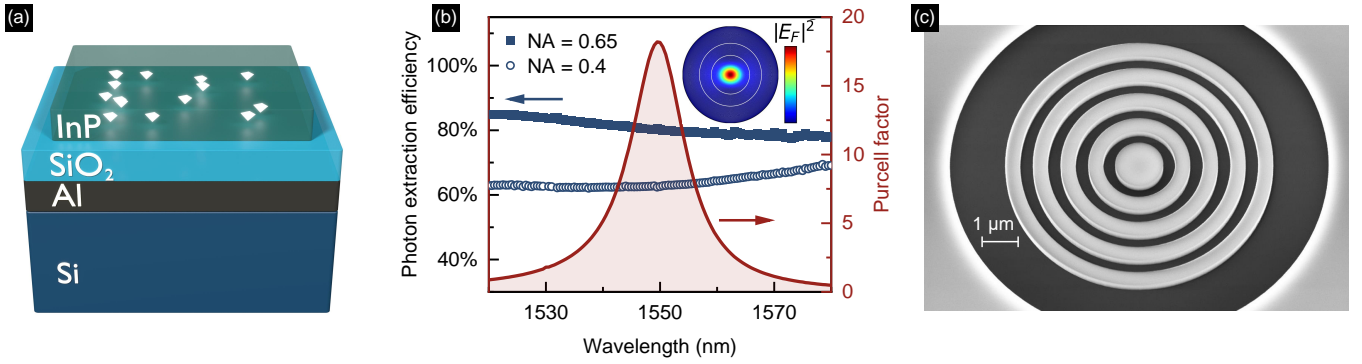


FIG. 1. Structure with QDs for imaging and optimized CBGs. **a**, The layer stack for efficient localization of single InAs/InP QDs emitting at C-band, **b**, calculated CBG Purcell factor (dark red line, right axis) and photon extraction efficiency (blue points, left axis). Inset: far-field emission pattern with rings marking NA = 0.4 and NA = 0.65. **c**, SEM image of a CBG cavity etched in InP on top of SiO₂.

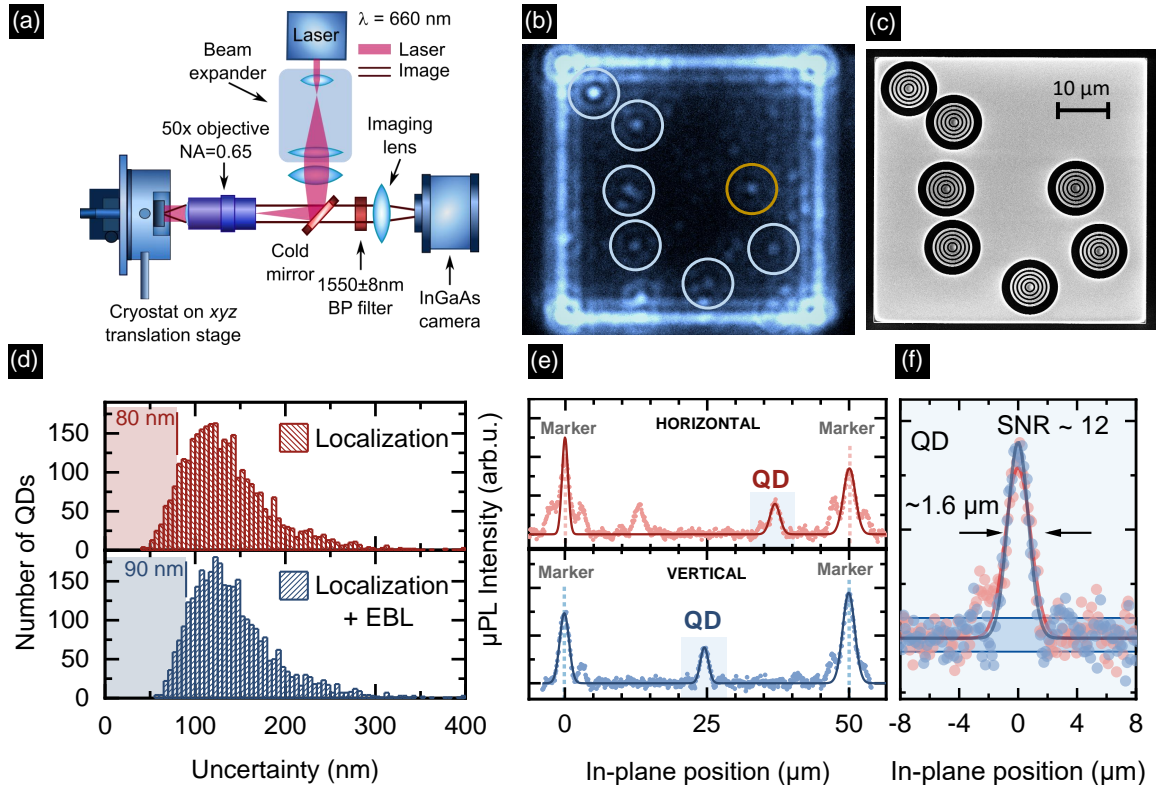


FIG. 2. μ PL imaging of the QDs. **a**, The optical setup used for imaging, **b**, a μ PL map of a $(50 \times 50) \mu\text{m}^2$ InP field containing seven localized InAs QDs emitting at C-band, **c**, SEM image of CBGs fabricated atop the localized and preselected QDs, **d**, histograms of QD localization accuracy (top) and overall cavity placement accuracy (bottom) for all detected spots, with markers for 10th distribution percentiles, **e**, exemplary μ PL map cross-sections showing the signal of the QD labeled with the orange circle in **b** and alignment marks together with Gaussian fits used for the QD localization, **f**, close-up of the QD signal from **e**, centered to 0 μm . The FWHM of the fitted Gaussian profiles is $\sim 1.6 \mu\text{m}$ and the signal-to-noise ratio (SNR) is 12.

1550nm band-pass filter with 8 nm full-width half-maximum (FWHM) placed in front of the imaging lens selects QDs with emission in the C-band.

Figure 2b shows a representative image of a field recorded with a camera integration time of 2.5 s. The QDs can clearly be recognized as individual bright spots with FWHM $\approx 1.6 \mu\text{m}$ (see Fig. 2f and **Supplemental Material**) and Airy rings

around. The square-shaped outline of the field scatters light and is used as AM for QD localization.

The localization of QDs is performed by taking vertical and horizontal cross-sections both crossing at a QD emission spot in the μ PL intensity map. Each cross-section thus contains the position of the target QD relative to two AMs (Fig. 2e). Gaussian profiles fitted to the QD and the AM signals are sub-

sequently used to determine the QD peak position relative to the AMs. The average signal-to-noise ratio for QD emission spots is 10.6, emphasizing the importance of the $7\times$ emission enhancement in the planar structure as compared to bulk InP. We find that for the brightest 10% of all QDs with $\text{SNR} > 15.5$, the position is fitted with an uncertainty of $< 54\text{ nm}$ in 1D and with an uncertainty of the AM position of $< 36\text{ nm}$, resulting in a total uncertainty of QD position in 1D of $< 62\text{ nm}$. In 2D, this translates to 80 nm accuracy for the QD localization. Finally, taking into account the EBL alignment accuracy of 40 nm as measured in our previous work¹⁶, we estimate the overall accuracy of 2D CBG placement to $\Delta R = 90\text{ nm}$. The histograms of QD localization accuracy and overall cavity placement accuracy for all detected spots are shown in Fig. 2d in the upper and lower panel, respectively, and the 80 nm and 90 nm levels are marked for reference. Medians for the distributions are slightly larger, 127 nm and 133 nm , due to processing of all detected spots, irrespective of their brightness and expected cavity fabrication precision. Details on the localization algorithm, derivation and discussion of the uncertainties, and data on the accuracy of cavity positioning are given in the **Supplemental Material**. Following the localization of suitable QDs, CBGs are fabricated using EBL with proximity error correction and an optimized inductively coupled plasma-reactive ion etching (ICP-RIE) process (see **Methods**). The SEM image presented in Fig. 2c is taken from the same field after fabricating the CBG cavities around pre-selected QDs indicated by the circles in Fig. 2b.

Characteristics of the fabricated devices

Process yield

We use a μPL setup to quantify the process yield that we define as the ratio between the number of QD-CBG devices with QD emission spectra matching the CBG mode and the number of all CBGs investigated, and we obtain $Y = 30\%$. This value should be compared with the yield that would be obtained in a statistical QD-CBG fabrication process. As we estimate the average number of QDs per field of size $F = 50\text{ }\mu\text{m}$ to $N_F = 10$, the probability of covering one of them with the central mesa of diameter $2R_0$ is $Y_{\text{random}} \sim N_F \times (2R_0/F)^2 = 0.67\% \ll Y$. Some of the QD (inside a CBG) emission spectra are significantly broadened (median linewidth of 0.76 nm , see **Supplemental Material**) as compared to the narrowest recorded linewidth of 0.14 nm (identical to the spectrometer resolution). We attribute the broadening to the impact of surface states and point defects caused by the cavity fabrication, effectively resulting in the spectral wandering of the QD emission line¹⁷. Such defects can as well introduce non-radiative recombination centers in the close vicinity of or even into the QD, quench the optical emission, and effectively reduce the process yield. Using the temperature-dependent μPL studies, we make sure that even the broadened emission lines follow the expected Varshni trend, ensuring that these spectral lines can indeed be associated with the QD emission as the temperature dependence of the cavity mode energy is much weaker.

Purcell enhancement

In the following, we discuss the optical properties of two exemplary devices, QD-CBG #1 and QD-CBG #2, each containing a single pre-selected QD coupled to the CBG cavity mode (see **Supplemental Material** for the properties of a third device QD-CBG #3). Figure 3a shows the narrow QD emission lines overlaid on the cavity mode with $Q = 194$, the latter obtained under high power cavity excitation, evidencing good spectral overlap between the cavity mode and the QD emission. We interpret the dominant QD emission lines in both devices as trions (CX), due to their linear intensity dependence on excitation power, and the lack of fine-structure splitting. This is in line with typical spectra for our InAs/InP QDs with preferential CX recombination where the average CX binding energy was measured to be 4.7 meV ¹⁰.

The coupling between the QD and the CBG cavity is evidenced by the observation of a reduced emission decay time as compared to the decay of QDs in the planar reference structure. For the CX line in QD-CBG #1 and #2 we record decay times of $\tau_{\#1} = (0.40 \pm 0.01)\text{ ns}$ and $\tau_{\#2} = (0.53 \pm 0.01)\text{ ns}$, respectively (Fig. 3b). To take statistical QD-to-QD fluctuations for the reference decay time into account, we estimate the average decay time of 8 uncoupled QD CX lines and obtain $\tau_{\text{ref}} = (1.99 \pm 0.16)\text{ ns}$, while the single reference shown in Fig. 3b has a decay time of $(2.01 \pm 0.02)\text{ ns}$. Therefore, the measured Purcell factor for QD-CBG #1 is $F_P = 5.0 \pm 0.4$ and $F_P = 3.8 \pm 0.3$ for QD-CBG #2. Although the obtained Purcell factors are comparable with $F_P = 3$ obtained in the non-deterministic fabrication approach⁹, we expect it to be much higher if the QD would perfectly match the cavity mode both spectrally and spatially. However, the expected Purcell factor decays rapidly with the dipole displacement \mathbf{r}_0 from the cavity center (decreases by half for $|\mathbf{r}_0| = 100\text{ nm}$), as the fabricated CBG is optimized for a higher-order mode that exhibits electric field minima along the cavity radial direction (see **Supplemental Material**). Hence, the relatively large total positioning uncertainty for QD-CBGs #1-#3 ($\Delta R \sim 140\text{--}150\text{ nm}$) and the non-ideal spectral emitter-cavity overlap explain the reduced F_P as compared to the model.

Photon extraction efficiency

We evaluate the photon extraction efficiency by recording the power-dependent μPL signal with a superconducting nanowire single-photon detector (SNSPD) in a calibrated optical setup (see Fig. 3c). The setup has a total transmission of $(1.1 \pm 0.2)\%$ (see **Supplemental Material**). The measured η values are corrected by the factor $\sqrt{1 - g^{(2)}(0)}$, to account for the detection of secondary photons due to the refilling of QD states^{18,19}. Here, the $g^{(2)}(0)$ value is obtained under the excitation power P_{sat} corresponding to saturation of the CX line. Evaluating the CX emission, we obtain an extraction efficiency $\eta_{\#1} = (16.6 \pm 2.7)\%$ for QD-CBG #1 and $\eta_{\#2} = (13.3 \pm 2.2)\%$ for QD-CBG #2 using an objective with $\text{NA} = 0.4$.

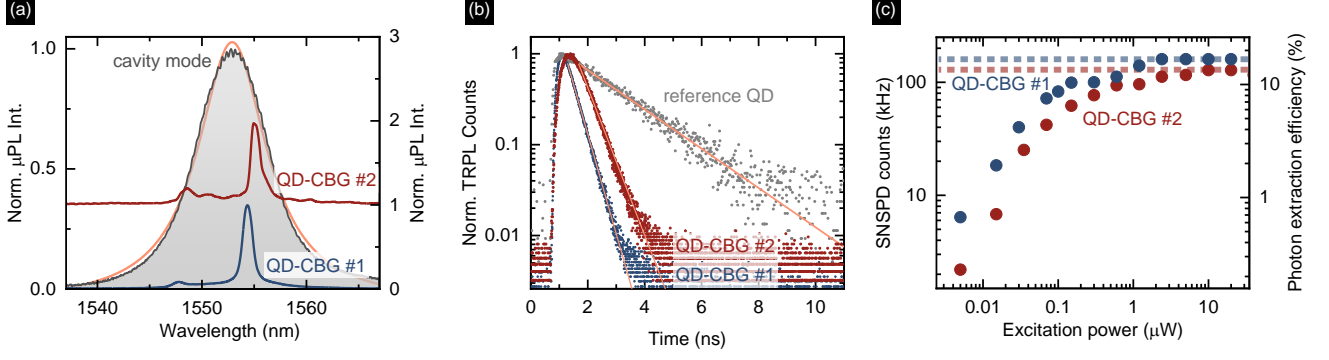


FIG. 3. Characteristics of exemplary fabricated devices, QD-CBGs #1 and #2. **a**, μ PL spectra for QDs in devices #1 and #2 overlaid on the cavity mode of device #2 (grey) and fitted with a Lorentzian profile (orange), stacked for clarity, **b**, time-resolved μ PL traces for these QDs with the reference QD decay, **c**, power-dependent count rates registered on the SNSPD detector. Horizontal lines mark the line μ PL signal saturation level used for the determination of photon extraction efficiency.

Single-photon emission purity

The photon statistics of a quantum light source are of fundamental importance for applications in photonic quantum technologies. In the following, we investigate the single-photon purity of the emission from QD-CBG #2 by analyzing the photon autocorrelation function $g^{(2)}(\tau)$ (cf. **Supplemental Material** for details on the data analysis and complementary $g^{(2)}(\tau)$ measurements).

Fig. 4a depicts the measured $g^{(2)}(\tau)$ histograms obtained under pulsed off-resonant excitation at a power $0.5 \times P_{\text{sat}}$ and LO-phonon-assisted, quasi-resonant excitation at $0.04 \times P_{\text{sat}}$ in the upper and lower panel, respectively. Under off-resonant excitation, the single-photon purity is limited by recapture processes resulting in $g^{(2)}(0)_{\text{fit}} = 0.05 \pm 0.02$, where the uncertainty is mainly determined by the background level B . From the fit, we determine a decay time of $\tau_{\text{dec}} = (0.67 \pm 0.03)$ ns, in good agreement with the spontaneous emission decay time observed in Fig. 3b ($\tau_{\text{#2}} = (0.53 \pm 0.01)$ ns).

Under weak quasi-resonant excitation at $P \ll P_{\text{sat}}$, the probability for charge-carrier recapture is strongly reduced, resulting in almost negligible background contributions ($B = 0$) (Fig. 4a, lower panel) and a fitted value of $g^{(2)}(0)_{\text{fit}} = (4.7 \pm 2.6) \times 10^{-3}$ at $P = 0.04 \times P_{\text{sat}}$. Additionally, we evaluated the raw antibunching value by integrating the raw coincidences around $\tau = 0$ over a full repetition period normalized by the Poisson level of the side peaks. This results in $g^{(2)}(0)_{\text{raw}} = (3.2 \pm 0.6) \times 10^{-3}$, with the error deduced from the standard deviation of the distribution of counts in the side peaks. As discussed later, this result compares favorably with previous reports on non-deterministically fabricated QD-CBGs.

Photon indistinguishability

Finally, we explore the photon indistinguishability of QD-CBG #2 by Hong-Ou-Mandel (HOM)-type two-photon inter-

ference (TPI) experiments²⁰ (see **Methods** and **Supplemental Material** for details on the experimental setup, data analysis, and complementary TPI measurements). The HOM histograms recorded for co- and cross-polarized measurement configurations are presented in Fig. 4b, and were obtained under pulsed quasi-resonant excitation with identical experimental conditions as the $g^{(2)}(\tau)$ measurement presented in the previous section (at $0.04 \times P_{\text{sat}}$). The data shown in Fig. 4b is not corrected for multi-photon events or contributions from residual laser light.

The HOM histograms feature a characteristic pattern that we analyze following the methodology described in Ref. 21. The reduced area of the central peak in the co-polarized measurement as compared to the maximally distinguishable cross-polarized measurement is a distinct signature of the two-photon coalescence due to a significant degree of photon-indistinguishability. From the width of the central dip we extract a photon coherence time of $T_2 = (103 \pm 13)$ ps. The visibility of the TPI is calculated from the ratio of the fitted central peak area in the co- and cross-polarized measurements as $V = 1 - A_{\text{Co}}/A_{\text{Cross}}$. We obtain a TPI visibility of $V = (19.3 \pm 2.6)\%$ with the accuracy being the propagated fitting errors reflecting the statistics of the experimental data. The temporally post-selected visibility at zero delay time ($\tau = 0$) is $V_{\text{PS}} = 99.8^{+0.2}_{-2.6}\%$, limited only by the system temporal response.

DISCUSSION

The scalable fabrication of active quantum photonic devices operating in the telecom C-band has been a long-standing challenge. This is mainly due to the random size and strain distribution of epitaxially grown QDs causing an inhomogeneous broadening of the emission and difficulties in localizing suitable QDs due to the high electronic noise level of detector arrays sensitive around $1.55 \mu\text{m}$ wavelength. In this work, we present a solution to this problem based on a hybrid sample design. We fabricate an InP layer containing epitaxial QDs on

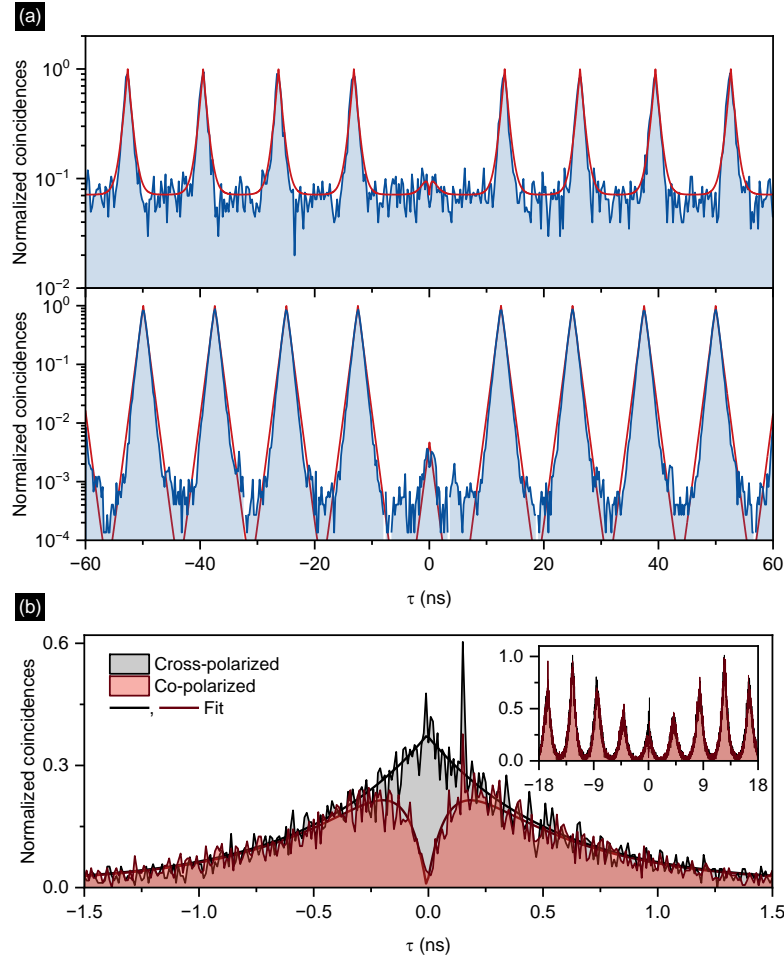


FIG. 4. Quantum optical experiments on QD-CBG #2. **a**, The second-order autocorrelation function $g^{(2)}(\tau)$ of the triggered photons for the above-band excitation (top), and LO-phonon-assisted quasi-resonant excitation (bottom), **b**, HOM histogram for cross- and co-polarized photons evidencing the indistinguishability by the two-photon interference visibility of $V = (19.3 \pm 2.6) \%$, and the post-selected value of $V_{PS} = 99.8^{+0.2}_{-2.6} \%$.

top of a Al reflector placed on a Si wafer carrier. This geometry significantly enhances the photon extraction efficiency from the QDs by a factor > 7 enabling the localization of single QDs in a wide-field imaging setup with a thermo-electrically cooled InGaAs camera. For the 10 % brightest QDs our setup achieves an imaging SNR > 15.5 and a localization uncertainty of ~ 80 nm with respect to alignment marks. After final EBL processing, we achieve an overall uncertainty of ~ 90 nm for fabricating a nano-photonic device around pre-selected QDs. The localization accuracy of our setup is comparable to setups operating in the 770-950 nm range (48 nm²², 30 nm²³) where Si-based sensors with four orders of magnitude lower electronic noise can be used. The accuracy in our setup can be further improved by using higher-NA objectives inside the cryostat together with an overall increased microscope magnification, which was reported to reduce the localization accuracy down to 5 nm²⁴. Alternatively, *in-situ* EBL²⁵ or photolithography²⁶ scanning techniques provide a similar accuracy down to ~ 35 nm, but are comparably slow, require cathodolumines-

cence signal for QD localization or, in case of photolithography, are not suitable to define reliably sub- μ m features.

To exemplify our approach, we fabricate CBG cavities with a resonance wavelength of 1.55 μ m around some of the pre-selected QDs. The QD-to-CBG coupling is evidenced by a Purcell factor of $F_P = 5.0 \pm 0.4$, further increasing the single-photon emission rate and final source brightness. Using our approach, we obtain a total process yield of 30 % for finding a pre-selected QD spectrally matching the CBG cavity, which is a significant improvement compared to the yield achievable with a random placement approach ($\sim 0.7 \%$). For our QD-CBG device, we measure a photon extraction efficiency of $(16.6 \pm 2.7) \%$ with a NA = 0.4 objective, which is comparable to previously reported devices probabilistically-fabricated and operating at C-band wavelengths⁹.

Our QD-CBG devices feature excellent single-photon emission purities with raw values down to $g^{(2)}(0) = (3.2 \pm 0.6) \times 10^{-3}$, beating previous records for non-deterministically fabricated QD-CBGs⁹, as well as most QDs

operating in the C-band^{27,28}, while being not yet competitive with the state-of-the-art²⁹.

Importantly, we report for the first time triggered TPI experiments for InP-based cavity-coupled QDs with emission wavelengths in the telecom C-band, which is crucial for applications in quantum information processing (QIP). We generate indistinguishable photons with a TPI visibility up to $V = (19.3 \pm 2.6)\%$ and a post-selected value of $V_{PS} = 99.8^{+0.2}_{-2.6}\%$ at zero time delay, setting a new record for QDs emitting in the C-band. Previous results in the C-band were based either on droplet epitaxy InAs/InP QDs in planar structures^{30,31} or InAs QDs grown on GaAs followed by an InGaAs metamorphic buffer, also located in planar structures^{32,33} or embedded in randomly placed CBGs⁹.

Further improvement in the photon indistinguishability is of utmost importance for applications in QIP. This is challenged by the strong coupling of QDs to their semiconductor environment via charge and spin noise, both causing QD decoherence^{21,34}. It is thus important to stabilize the QD environment, e. g. via electrical gates. In combination with coherent pumping schemes, such as two-photon resonant excitation, we expect a further improvement of the photon coherence time and hence indistinguishability³⁵.

Moreover, the InP material system used in our work appears to be advantageous for QD-based quantum photonic devices operating in the C-band and compared to GaAs-based devices. Despite the careful strain engineering involved in the epitaxy of QDs on GaAs³⁶, the metamorphic buffer complicates the device engineering and QD growth. In contrast, an unstrained InP system is free from threading dislocations that would be a source of dangling bonds causing non-radiative recombination, thus lowering the efficiency³⁷.

In conclusion, our work opens the route for the scalable fabrication of telecom C-band wavelength quantum photonic devices with QDs delivering flying qubits, i.e. single or entangled photons³⁸, or acting as a non-linear element for QIP³⁹. Improvements in our optical imaging setup will further increase the device yield and positioning accuracy, while the electric control and coherent excitation of QD emitters will further push the achievable photon-indistinguishability.

Methods

Epitaxial growth and fabrication of planar structure with QDs– The fabrication of the QD-CBG devices starts with the MOVPE growth of low-density Stranski-Krastanov InAs/InP QDs emitting in the C-band¹². Then, the applied process analogous to the one described in Ref. 10 results in the structure consisting of a thin InP layer with QDs over SiO₂ and Al, heterogeneously integrated with a Si carrier wafer using BCB and ready for imaging. Further details are given in **Supplemental Material**.

Modeling of the CBG– The QD is modeled as a classical dipole⁴⁰, and the numerical simulations of the CBG geometry are performed using a modal method employing a true open boundary condition⁴¹. See the **Supplemental Material** for further details.

Deterministic fabrication of QD-CBG devices– After the μ PL imaging step, introduced in the Results section and elaborated in **Supplemental Material**, the CBG cavities are fabricated via e-beam lithography using high-precision alignment based on the InP mark detection in JEOL JBX-9500FSZ e-beam writer. This step is followed by HBr-based ICP-RIE etching, using CSAR resist and a PECVD-deposited SiN_x hard mask. The calculated design is first scaled and fabricated using a nominally identical heterostructure to investigate the mode energy vs. size dependence and to account for the fabrication imperfections. Additionally, we experimentally determine the ~ 15 nm temperature-induced blueshift of the mode energy between a room and low temperature resulting from the contraction of the structure (introducing size and strain changes), as well as from the change of the refractive indices of the layers.

Optical characterization of devices– The structure with QD-CBG devices is held in

a helium-flow cryostat allowing for control of the sample temperature in the range of 4.2–300 K. For our standard μ PL studies, the structures are optically excited through a microscope objective with NA = 0.4 or 0.65 and 20 \times magnification using 660 nm or 805 nm light generated with semiconductor laser diodes. The same objective is used to collect the μ PL signal and to direct it for spectral analysis into a 1 m-focal-length monochromator equipped with a liquid-nitrogen-cooled InGaAs multichannel array detector, providing spatial and spectral resolution of $\sim 2 \mu\text{m}$ and $\sim 25 \mu\text{eV}$, respectively.

The photon extraction efficiency and time-resolved μ PL are measured in the same setup. Here, QDs are excited by ~ 50 ps-long pulses with a repetition rate of 80 MHz and a central wavelength of 805 nm. At the same time, the second monochromator output port is equipped with the fiber coupling system, transmitting the signal to an NbN-based SNSPD (Scontel) with $\sim 87\%$ quantum efficiency in the range 1.5–1.6 μm and ~ 200 dark counts per second. A multichannel picosecond event timer (PicoHarp 300 by PicoQuant GmbH) analyzes the single photon counts as a time-to-amplitude converter. The overall time resolution of the setup is ~ 80 ps. Experimental setups, and data on the setup transmission efficiency used for determining the photon extraction efficiency are given in **Supplemental Material**.

Photon autocorrelation measurements– For the photon-autocorrelation measurements, QD-CBG devices were optically excited using a Ti:Sapphire (Ti:Sa) laser (Coherent Mira-HP) or a widely tunable ps-pulsed laser system based on an optical parametric oscillator (OPO) (picoEmerald by APE GmbH) with repetition rates of 76 MHz and 80 MHz, respectively. We use a fiber-coupled bandpass filter (FWHM = ~ 0.4 nm) for spectrally selecting the QD emission, followed by a 50:50 fiber beam splitter. For the off-resonant excitation, we use a microscope objective with NA = 0.7 and 100 \times magnification and excite the QD emission with ~ 2 ps-long pulses at 830 nm from the Ti:Sa. The signal is detected with a pair of SNSPDs with $\sim 87\%$ and $\sim 92\%$ quantum efficiency at 1550 nm. For the quasi-resonant excitation, we use an aspheric lens (NA = 0.6) mounted inside a low-vibration closed-cycle cryostat (attoDRY800 by Attocube Systems AG) cooled to 4.5 K. Here, the OPO-laser is used and adjusted to a pulse length of 5 ps. Single photons are detected via SNSPDs with 80% detection efficiency at 1550 nm and 57 ps timing jitter (complete system temporal response). The excitation energy was determined in photoluminescence excitation experiments to be 0.83537 eV (37.57 meV above the QD emission energy, cf. **Supplemental Material**), which was also used for following TPI experiments.

Photon-indistinguishability measurements– In the TPI experiments, an additional 4 ns delay was introduced between consecutive laser pulses by adding an imbalanced free-space Mach-Zehnder interferometer (MZI) in the excitation path, which was compensated in the HOM setup on the detection side. Hence, the excitation sequence is composed of pairs of pulses separated by 4 ns, every 12.5 ns corresponding to 80 MHz laser repetition rate. Free-space waveplates were used to match the polarization for the TPI inside the fiber beam splitter. The exact polarization was set by using a polarimeter at the beam splitter output in combination with a laser tuned to the QD emission wavelength. Fine-tuning the relative delay between both MZI arms was used to precisely match the detection and excitation delay, respectively. The contrast of classical Michelson interference of the laser with itself was used for optimization. See **Supplemental Material** for the scheme of the experimental setup and the details of the HOM data analysis.

Acknowledgements

The authors acknowledge financial support from the Danish National Research Foundation via the Research Centers of Excellence NanoPhoton (DNRF147) and the Center for Macroscopic Quantum States bigQ (DNRF142). P. H. was funded by the Polish National Science Center within the Etyuda 8 scholarship (Grant No. 2020/36/T/ST5/00511) and by the European Union under the European Social Fund. D. A. V. and T. H. acknowledge financial support by the German Federal Ministry of Education and Research (BMBF) via the project “QuSecure” (Grant No. 13N14876) within the funding program Photonic Research Germany, the BMBF joint project “tubLAN Q.O” (Grant No. 16KISQ087K), and by the Einstein Foundation via the Einstein Research Unit “Quantum Devices”. P. M. acknowledges the financial support from the Polish National Science Center (Grant No. 2020/39/D/ST5/02952). N. G. acknowledges support from the European Research Council (ERC-CoG “UNITY”, Grant No. 865230), and from the Independent Research Fund Denmark (Grant No. DFF-9041-00046B).

Funding Sources

Danish National Research Foundation: DNRF147, DNRF142; Polish National Science Center: 2020/36/T/ST5/00511; 2020/39/D/ST5/02952 European Union: European Social Fund; European Research Council: 865230; Independent Research Fund Denmark: DFF-9041-00046B German Federal Ministry of Education and Research: 13N14876, 16KISQ087K; Einstein Foundation: Einstein Research Unit “Quantum Devices”.

Supplemental Material

The description of device fabrication, numerical simulations, extended data for QD localization algorithm and uncertainty analysis, optical characterization of the devices, evaluation of single-photon purity, and the analysis of the two-photon-interference measurements.

¹H. J. Kimble, “The quantum internet,” *Nature* **453**, 1023–1030 (2008).

²N. Gisin, G. Ribordy, W. Tittel, and H. Zbinden, “Quantum cryptography,” *Rev. Modern Phys.* **74**, 145–195 (2002).

- ³D. A. Vajner, L. Rickert, T. Gao, K. Kaymazlar, and T. Heindel, "Quantum communication using semiconductor quantum dots," *Adv. Quantum Technol.* **5**, 2100116 (2022).
- ⁴A. Serafini, S. Mancini, and S. Bose, "Distributed quantum computation via optical fibers," *Phys. Rev. Lett.* **96**, 010503 (2006).
- ⁵Y. Cao, Y. Zhao, Q. Wang, J. Zhang, S. X. Ng, and L. Hanzo, "The Evolution of Quantum Key Distribution Networks: On the Road to the Qinternet," *IEEE Communications Surveys & Tutorials* **24**, 839–894 (2022).
- ⁶O. Gazzano, S. M. de Vasconcellos, C. Arnold, A. Nowak, E. Galopin, I. Sagnes, L. Lanco, A. Lemaître, and P. Senellart, "Bright solid-state sources of indistinguishable single photons," *Nat. Commun.* **4**, 1425 (2013).
- ⁷N. Tomm, A. Javadi, N. O. Antoniadis, D. Najer, M. C. Löbl, A. R. Korsch, R. Schott, S. R. Valentin, A. D. Wieck, A. Ludwig, and R. J. Warburton, "A bright and fast source of coherent single photons," *Nat. Nanotechnol.* **16**, 399–403 (2021).
- ⁸H. Wang, Z.-C. Duan, Y.-H. Li, S. Chen, J.-P. Li, Y.-M. He, M.-C. Chen, Y. He, X. Ding, C.-Z. Peng, C. Schneider, M. Kamp, S. Höfling, C.-Y. Lu, and J.-W. Pan, "Near-transform-limited single photons from an efficient solid-state quantum emitter," *Phys. Rev. Lett.* **116**, 213601 (2016).
- ⁹C. Nawrath, R. Joos, S. Kolatschek, S. Bauer, P. Pruy, F. Hornung, J. Fischer, J. Huang, P. Vijayan, R. Sittig, M. Jetter, S. L. Portalupi, and P. Michler, "High emission rate from a Purcell-enhanced, triggered source of pure single photons in the telecom C-band," (2022), [arXiv:2207.12898 \[quant-ph\]](https://arxiv.org/abs/2207.12898).
- ¹⁰P. Holewa, A. Sakanas, U. M. Gür, P. Mrowiński, A. Huck, B.-Y. Wang, A. Musiał, K. Yvind, N. Gregersen, M. Syperek, and E. Semenova, "Bright Quantum Dot Single-Photon Emitters at Telecom Bands Heterogeneously Integrated on Si," *ACS Photonics* **9**, 2273–2279 (2022).
- ¹¹S. Liu, K. Srinivasan, and J. Liu, "Nanoscale positioning approaches for integrating single solid-state quantum emitters with photonic nanostructures," *Laser Photonics Rev.* **15**, 2100223 (2021).
- ¹²Y. Berdnikov, P. Holewa, S. Kadhodazadeh, J. M. Śmigiel, A. Frackowiak, A. Sakanas, K. Yvind, M. Syperek, and E. Semenova, "Fine-tunable near-critical Straniski-Krastanov growth of InAs/InP quantum dots," (2023), [arXiv:2301.11008 \[cond-mat.mes-hall\]](https://arxiv.org/abs/2301.11008).
- ¹³A. Barbiero, J. Huwer, J. Skiba-Szymanska, T. Müller, R. M. Stevenson, and A. J. Shields, "Design study for an efficient semiconductor quantum light source operating in the telecom C-band based on an electrically-driven circular Bragg grating," *Opt. Express* **30**, 10919 (2022).
- ¹⁴L. Bremer, C. Jimenez, S. Thiele, K. Weber, T. Huber, S. Rodt, A. Herkommer, S. Burger, S. Höfling, H. Giessen, and S. Reitzenstein, "Numerical optimization of single-mode fiber-coupled single-photon sources based on semiconductor quantum dots," *Opt. Express* **30**, 15913 (2022).
- ¹⁵L. Rickert, F. Betz, M. Plock, S. Burger, and T. Heindel, "High-performance designs for fiber-pigtailed quantum-light sources based on quantum dots in electrically-controlled circular Bragg gratings," *Opt. Express* (2023), [10.1364/oe.486060](https://doi.org/10.1364/oe.486060).
- ¹⁶A. Sakanas, E. Semenova, L. Ottaviano, J. Mørk, and K. Yvind, "Comparison of processing-induced deformations of InP bonded to Si determined by e-beam metrology: Direct vs. adhesive bonding," *Microelectron. Eng.* **214**, 93–99 (2019).
- ¹⁷J. Liu, K. Konthasinghe, M. Davanço, J. Lawall, V. Anant, V. Verma, R. Mirin, S. W. Nam, J. D. Song, B. Ma, Z. S. Chen, H. Q. Ni, Z. C. Niu, and K. Srinivasan, "Single self-assembled InAs/GaAs quantum dots in photonic nanostructures: The role of nanofabrication," *Phys. Rev. Applied* **9**, 064019 (2018).
- ¹⁸J. Yang, C. Nawrath, R. Keil, R. Joos, X. Zhang, B. Höfer, Y. Chen, M. Zopf, M. Jetter, S. L. Portalupi, F. Ding, P. Michler, and O. G. Schmidt, "Quantum dot-based broadband optical antenna for efficient extraction of single photons in the telecom O-band," *Opt. Express* **28**, 19457 (2020).
- ¹⁹H. Kumano, T. Harada, I. Suemune, H. Nakajima, T. Kuroda, T. Mano, K. Sakoda, S. Odashima, and H. Sasakura, "Stable and efficient collection of single photons emitted from a semiconductor quantum dot into a single-mode optical fiber," *Appl. Phys. Express* **9**, 032801 (2016).
- ²⁰C. K. Hong, Z. Y. Ou, and L. Mandel, "Measurement of subpicosecond time intervals between two photons by interference," *Phys. Rev. Lett.* **59**, 2044–2046 (1987).
- ²¹A. Thoma, P. Schnauber, M. Gschrey, M. Seifried, J. Wolters, J. H. Schulze, A. Strittmatter, S. Rodt, A. Carmele, A. Knorr, T. Heindel, and S. Reitzenstein, "Exploring dephasing of a solid-state quantum emitter via time- and temperature-dependent Hong-Ou-Mandel experiments," *Phys. Rev. Lett.* **116**, 1–5 (2016).
- ²²T. Kojima, K. Kojima, T. Asano, and S. Noda, "Accurate alignment of a photonic crystal nanocavity with an embedded quantum dot based on optical microscopic photoluminescence imaging," *Appl. Phys. Lett.* **102**, 011110 (2013).
- ²³L. Sapienza, M. Davanço, A. Badolato, and K. Srinivasan, "Nanoscale optical positioning of single quantum dots for bright and pure single-photon emission," *Nat. Commun.* **6**, 7833 (2015).
- ²⁴J. Liu, M. I. Davanço, L. Sapienza, K. Konthasinghe, J. V. D. M. Cardoso, J. D. Song, A. Badolato, and K. Srinivasan, "Cryogenic photoluminescence imaging system for nanoscale positioning of single quantum emitters," *Rev. Sci. Instrum.* **88**, 023116 (2017).
- ²⁵M. Gschrey, A. Thoma, P. Schnauber, M. Seifried, R. Schmidt, B. Wohlfeil, L. Krüger, J.-H. Schulze, T. Heindel, S. Burger, F. Schmidt, A. Strittmatter, S. Rodt, and S. Reitzenstein, "Highly indistinguishable photons from deterministic quantum-dot microlenses utilizing three-dimensional in situ electron-beam lithography," *Nat. Commun.* **6**, 7662 (2015).
- ²⁶A. Dousse, L. Lanco, J. Suffczyński, E. Semenova, A. Miard, A. Lemaître, I. Sagnes, C. Roblin, J. Bloch, and P. Senellart, "Controlled light-matter coupling for a single quantum dot embedded in a pillar microcavity using far-field optical lithography," *Phys. Rev. Lett.* **101**, 30–33 (2008).
- ²⁷K. Takemoto, Y. Nambu, T. Miyazawa, Y. Sakuma, T. Yamamoto, S. Yorozu, and Y. Arakawa, "Quantum key distribution over 120 km using ultrahigh purity single-photon source and superconducting single-photon detectors," *Sci. Rep.* **5**, 14383 (2015).
- ²⁸K. D. Zeuner, K. D. Jöns, L. Schweickert, C. R. Hedlund, C. N. Lobato, T. Lettner, K. Wang, S. Gyger, E. Schöll, S. Steinhauer, M. Hammar, and V. Zwiller, "On-Demand Generation of Entangled Photon Pairs in the Telecom C-Band with InAs Quantum Dots," *ACS Photonics* **8**, 2337–2344 (2021).
- ²⁹T. Miyazawa, K. Takemoto, Y. Nambu, S. Miki, T. Yamashita, H. Terai, M. Fujiwara, M. Sasaki, Y. Sakuma, M. Takatsu, T. Yamamoto, and Y. Arakawa, "Single-photon emission at 1.5 μm from an InAs/InP quantum dot with highly suppressed multi-photon emission probabilities," *Appl. Phys. Lett.* **109**, 132106 (2016).
- ³⁰M. Anderson, T. Müller, J. Skiba-Szymanska, A. B. Krysa, J. Huwer, R. M. Stevenson, J. Heffernan, D. A. Ritchie, and A. J. Shields, "Coherence in single photon emission from droplet epitaxy and Straniski-Krastanov quantum dots in the telecom C-band," *Appl. Phys. Lett.* **118**, 014003 (2021).
- ³¹L. Wells, T. Müller, R. M. Stevenson, J. Skiba-Szymanska, D. A. Ritchie, and A. J. Shields, "Coherent light scattering from a telecom C-band quantum dot," (2022), [arXiv:2205.07997 \[quant-ph\]](https://arxiv.org/abs/2205.07997).
- ³²C. Nawrath, F. Olbrich, M. Paul, S. L. Portalupi, M. Jetter, and P. Michler, "Coherence and indistinguishability of highly pure single photons from non-resonantly and resonantly excited telecom C-band quantum dots," *Appl. Phys. Lett.* **115**, 023103 (2019).
- ³³C. Nawrath, H. Vural, J. Fischer, R. Schaber, S. L. Portalupi, M. Jetter, and P. Michler, "Resonance fluorescence of single In(Ga)As quantum dots emitting in the telecom C-band," *Appl. Phys. Lett.* **118**, 244002 (2021).
- ³⁴A. V. Kuhlmann, J. Houel, A. Ludwig, L. Greuter, D. Reuter, A. D. Wieck, M. Poggio, and R. J. Warburton, "Charge noise and spin noise in a semiconductor quantum device," *Nature Physics* **9**, 570–575 (2013).
- ³⁵A. Reigue, R. Hosten, and V. Voliotis, "Resonance fluorescence of a single semiconductor quantum dot: the impact of a fluctuating electrostatic environment," *Semicond. Sci. Technol.* **34**, 113001 (2019).
- ³⁶R. Sittig, C. Nawrath, S. Kolatschek, S. Bauer, R. Schaber, J. Huang, P. Vijayan, P. Pruy, S. L. Portalupi, M. Jetter, and P. Michler, "Thin-film InGaAs metamorphic buffer for telecom C-band InAs quantum dots and optical resonators on GaAs platform," *Nanophotonics* **11**, 1109–1116 (2022).
- ³⁷L. Seravalli, G. Trevisi, P. Frigeri, D. Rivas, G. Muñoz-Matutano, I. Suárez, B. Alén, J. Canet-Ferrer, and J. P. Martínez-Pastor, "Single quantum dot emission at telecom wavelengths from metamorphic InAs/InGaAs nanostructures grown on GaAs substrates," *Appl. Phys. Lett.* **98**, 173112 (2011).
- ³⁸C.-Y. Lu and J.-W. Pan, "Quantum-dot single-photon sources for the quantum internet," *Nat. Nanotechnol.* **16**, 1294–1296 (2021).
- ³⁹A. Javadi, I. Söllner, M. Arcari, S. L. Hansen, L. Midolo, S. Mahmoodian, G. Kiršanskė, T. Pregolato, E. H. Lee, J. D. Song, S. Stobbe, and P. Lodahl, "Single-photon non-linear optics with a quantum dot in a waveguide," *Nat. Commun.* **6**, 8655 (2015).
- ⁴⁰L. Novotny and B. Hecht, *Principles of Nano-Optics*, 2nd ed. (Cambridge

University Press, 2012).

⁴¹U. M. Gür, S. Arslanagić, M. Mattes, and N. Gregersen, “Open-geometry

modal method based on transverse electric and transverse magnetic mode expansion for orthogonal curvilinear coordinates,” [Phys. Rev. E **103**, 033301 \(2021\)](#).

Supplemental Material

Scalable quantum photonic devices emitting indistinguishable photons in the telecom C-band

Paweł Holewa,^{1,2,3,*} Emilia Zięba-Ostójk,¹ Daniel A. Vajner,⁴ Maja Wasiluk,¹ Benedek Gaál,² Aurimas Sakanas,² Marek Burakowski,¹ Paweł Mrowiński,¹ Bartosz Krajnik,¹ Meng Xiong,^{2,3} Alexander Huck,⁵ Kresten Yvind,^{2,3} Niels Gregersen,² Anna Musiał,¹ Tobias Heindel,⁴ Marcin Syperek,^{1,†} and Elizaveta Semenova^{2,3,‡}

¹*Department of Experimental Physics, Faculty of Fundamental Problems of Technology, Wrocław University of Science and Technology, Wyb. Wyspiańskiego 27, 50-370 Wrocław, Poland*

²*DTU Electro, Department of Electrical and Photonics Engineering, Technical University of Denmark, Kongens Lyngby 2800, Denmark*

³*NanoPhoton-Center for Nanophotonics, Technical University of Denmark, 2800 Kongens Lyngby, Denmark*

⁴*Institute of Solid State Physics, Technische Universität Berlin, 10623 Berlin, Germany*

⁵*Center for Macroscopic Quantum States (bigQ), Department of Physics, Technical University of Denmark, 2800 Kongens Lyngby, Denmark*

CONTENTS

S-I. Optical simulations of the cavity geometry	S-2
S-II. Nanofabrication of the devices	S-3
A. MOVPE growth of InAs/InP quantum dots	S-3
B. Fabrication of the sample for μ PL imaging	S-4
C. Deterministic fabrication of the cavities	S-4
S-III. Accuracy of determination of QD positions from μ PL maps and final cavity positioning	S-4
A. Signal-to-noise ratio	S-4
B. Localization algorithm	S-5
C. Uncertainty of scaling the μ PL maps	S-6
D. Image rotation ϕ	S-6
E. One-dimensional QD position ΔQ_i	S-7
F. Two-dimensional QD position ΔQ	S-7
G. Distance between QD position and cavity center R – accuracy of cavity positioning ΔR	S-7
H. Example calculations for QD-CBGs #1–#3	S-8
I. Calculation of the diffraction-limited spot size	S-8
J. Statistics on QD spot size and the accuracy of QD positioning	S-8
S-IV. Optical setups	S-10
S-V. Determination of the photon extraction efficiency	S-10
S-VI. Supporting μ PL data for QD-CBG devices	S-11
A. QD linewidths	S-11
B. Time-resolved μ PL	S-12
C. Temperature-dependent μ PL	S-12
S-VII. Quantum optics experiments	S-13
A. Off-resonant autocorrelation data for QD-CBG #2	S-13
B. Microphotoluminescence excitation spectroscopy of QD-CBG #2	S-14
C. Quasi-resonant autocorrelation data for QD-CBG #2	S-14
D. Indistinguishability measurements and data analysis	S-16

* pawel.holewa@pwr.edu.pl

† marcin.syperek@pwr.edu.pl

‡ esem@fotonik.dtu.dk

S-I. OPTICAL SIMULATIONS OF THE CAVITY GEOMETRY

The CBG geometry is modeled using a modal method employing a true open geometry boundary condition [1]. Here, the geometry is divided into uniform layers along a propagation z axis, and the field is expanded in eigenmodes of each uniform layer. The QD is modeled as a classical dipole emitter using the equivalence principle [2]. The eigenmode expansion coefficients in the QD layer are computed using the reciprocity theorem [3], and the fields are connected at each layer interface using the S matrix formalism [3, 4].

We model the Purcell factor $F_P = P/P_0$ as the power P emitted by the classical dipole relative to the power P_0 in a bulk medium. The power P and the electric near field $\mathbf{E}(\mathbf{r})$ generated by a dipole \mathbf{d} with frequency ω_0 at the position \mathbf{r}_0 can be written in terms of the optical Green's function $\overleftrightarrow{\mathbf{G}}(\mathbf{r}, \mathbf{r}')$ as [2]

$$P(\mathbf{r}_0) = \frac{\omega_0^3 \mu_0 |\mathbf{d}|^2}{2} \text{Im} \left(\mathbf{n}_d^* \cdot \overleftrightarrow{\mathbf{G}}(\mathbf{r}_0, \mathbf{r}_0) \cdot \mathbf{n}_d \right) \quad (\text{S1})$$

$$\mathbf{E}(\mathbf{r}) = \omega_0^2 \mu_0 \overleftrightarrow{\mathbf{G}}(\mathbf{r}, \mathbf{r}_0) \mathbf{d}, \quad (\text{S2})$$

where $\mathbf{n}_d = \mathbf{d}/|\mathbf{d}|$ is the dipole orientation. The corresponding far field $P_{\text{FF}}(\theta, \varphi, \mathbf{r}_0)$ is then determined from Eq. (S2) using a standard near field to far field transformation [5]. The total collected power P_{Lens} detected by the lens with a given numerical aperture (NA) is obtained by integration of $P_{\text{FF}}(\theta, \varphi, \mathbf{r}_0)$ over the unit solid angle Ω as

$$P_{\text{Lens}}(\mathbf{r}_0) = \int_{\theta < \theta_{\text{NA}}} P_{\text{FF}}(\theta, \varphi, \mathbf{r}_0) d\Omega, \quad (\text{S3})$$

where θ_{NA} is defined by the NA of the lens. Finally, the extraction efficiency is defined as $\eta = P_{\text{Lens}}/P$.

The dominant lines in all investigated QD-CBG devices are trions (CX) which emit circularly polarized photons (σ^\pm). We thus model the trion state dipole orientation as

$$\mathbf{n}_d = \mathbf{n}_{\text{CX}} = \frac{1}{\sqrt{2}}(\mathbf{r} \pm i\varphi), \quad (\text{S4})$$

where \mathbf{r} and φ are unit vectors of the cylindrical coordinate system. Inserting Eq. (S4) into Eq. (S1), we obtain the power P_{CX} emitted by the trion given by

$$P_{\text{CX}}(\mathbf{r}_0) = \frac{P_r(\mathbf{r}_0) + P_\varphi(\mathbf{r}_0)}{2}, \quad (\text{S5})$$

where P_r (P_φ) is the power emitted by a dipole at position \mathbf{r}_0 oriented along the r (φ) axis. Similarly, the far field generated by the trion becomes

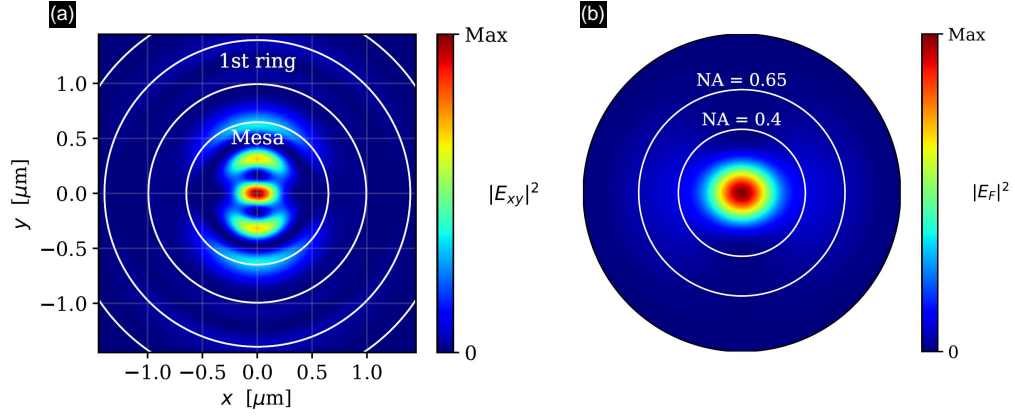
$$P_{\text{FF,CX}}(\theta, \varphi, \mathbf{r}_0) = \frac{1}{2} (P_{\text{FF},r}(\theta, \varphi, \mathbf{r}_0) + P_{\text{FF},\varphi}(\theta, \varphi, \mathbf{r}_0)), \quad (\text{S6})$$

where r and φ again refer to far fields generated by the two dipole orientations. Finally, the total photon extraction efficiency for the trion at the position \mathbf{r}_0 becomes

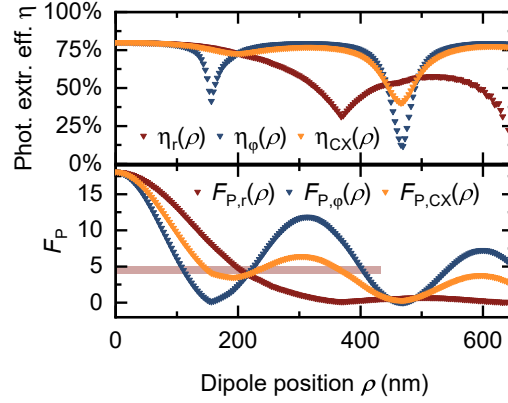
$$\eta_{\text{CX}}(\mathbf{r}_0) = \frac{P_{\text{Lens,CX}}(\mathbf{r}_0)}{P_{\text{CX}}(\mathbf{r}_0)} = \frac{P_{\text{Lens},r}(\mathbf{r}_0) + P_{\text{Lens},\varphi}(\mathbf{r}_0)}{P_r(\mathbf{r}_0) + P_\varphi(\mathbf{r}_0)}. \quad (\text{S7})$$

The near and far fields for the cavity mode are presented in Supplementary Fig. S1. The near-field profile shown in Supplementary Fig. S1a evidences the higher-order nature of the optimized cavity mode characteristic of the bullseye design [6].

The extraction efficiency η and Purcell factor F_P computed using Eq. (S5) and Eq. (S7) as a function of spatial misalignment ρ of the QD is presented in Supplementary Fig. S2. Whereas the photon extraction efficiency overall displays robustness towards misalignment, the decay of the Purcell factor with ρ is much more pronounced. The variations of F_P along the r and φ axes are quite different and result from the different variations of the field profile shown in Supplementary Fig. S1 along the x and y axes.



Supplementary Fig. S1. **a**, Near field and **b**, far field mode profiles of the CBG with 4 rings generated by a linear dipole $\mathbf{n}_d = \mathbf{r}$.



Supplementary Fig. S2. QD displacement tolerance: The photon extraction efficiency $\eta(\rho)$ (top) and Purcell factor $F_P(\rho)$ (bottom) as a function of the dipole-center separation ρ computed for the r , ϕ and CX dipole orientations.

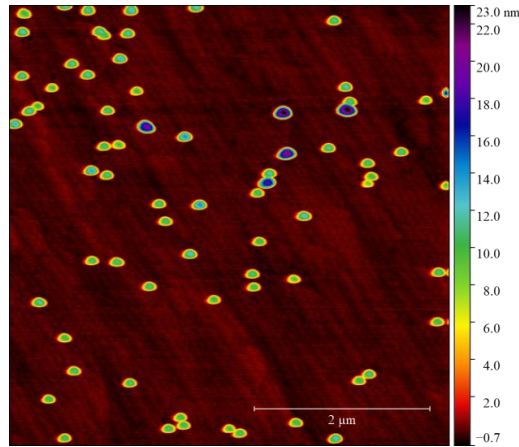
S-II. NANOFABRICATION OF THE DEVICES

In this section, we present the details of the fabrication flow applied to realize the circular Bragg gratings with quantum dots. The fabrication of the structure is similar to the one presented in Ref. [7].

A. MOVPE growth of InAs/InP quantum dots

We start with the epi-ready InP wafer and grow the InGaAs etch stop and InP layers on a (001)-oriented InP substrate in the low-pressure metalorganic vapor-phase epitaxy (MOVPE) TurboDisc® reactor using arsine (AsH_3), phosphine (PH_3), tertiarybutylphosphine (TBP) and trimethylindium (TMIn) precursors with H_2 as a carrier gas. We grow the 0.5 μm -thick InP buffer and 200 nm-thick $\text{In}_{0.53}\text{Ga}_{0.47}\text{As}$ lattice-matched to InP at 610 $^\circ\text{C}$ and a 156 nm-thick InP layer. Then, the temperature is decreased to 493 $^\circ\text{C}$, stabilized under TBP for 180 s and AsH_3 for 27 s. The nucleation of QDs occurs in the Stranski-Krastanov growth mode after deposition of nominally 1.22 ML-thick InAs at growth rate 0.53 ML/s under TMIn and AsH_3 flow rates of 11.8 $\mu\text{mol}/\text{min}$ and 590 $\mu\text{mol}/\text{min}$, respectively (V/III ratio of 50). Nucleated QDs are annealed for 3.5 s at the growth temperature in AsH_3 ambient before the deposition of a 156 nm-thick InP capping layer (12 nm at 493 $^\circ\text{C}$, and the remaining 144 nm after increasing the temperature up to 610 $^\circ\text{C}$) what finishes the growth sequence.

Supplementary Figure S3 presents the atomic force microscopy (AFM) image of a reference structure that has the same InAs/InP quantum dots (grown under nominally same conditions) without InGaAs sacrificial layer and metallic mirror (no processing was done on this structure). We estimate the density of QDs to be $3.1 \times 10^8/\text{cm}^2$ at the center of the wafer where the



Supplementary Fig. S3. AFM image of the InP surface with InAs QDs grown in MOVPE under nominally the same conditions as those used for the imaging.

imaging fields are fabricated.

B. Fabrication of the sample for μ PL imaging

Afterwards, SiO_2 is deposited in plasma-enhanced chemical vapor deposition (PECVD). This layer is intended to be 358.6 nm-thick. We cover it with a 120 nm-thick Al layer deposited via electron-beam evaporation. We bond the flipped structure to the Si chip carrier utilizing spin-coated AP3000 adhesion promoter and benzocyclobutene (BCB) on Si and AP3000 on the InP wafer. The bonding is done by applying the force of ~ 2 kN in vacuum at 250 $^\circ\text{C}$. The substrate removal step is done by ~ 60 min dip in HCl and the InGaAs etch-stop layer is subsequently removed in $\text{H}_2\text{SO}_4:\text{H}_2\text{O}_2:\text{H}_2\text{O}=1:8:80$ mixture.

Next, by employing electron-beam lithography (EBL) followed by inductively coupled plasma-reactive ion etching (ICP-RIE) to etch InP down to SiO_2 , we fabricate square imaging fields with 50 μm side-length and alignment marks (AMs) dedicated to EBL outside the fields. Therefore, we have different AMs for optical imaging (edges of the imaging fields) and for EBL alignment marks detection (InP crosses). This approach is justified by the simplification of the fabrication flow, as we do not deposit metallic AMs, relying instead on the outline of the field visible due to the μPL signal scattering from its edges. We check also that the material contrast between InP and SiO_2/Al regions is sufficient for the AM detection during the EBL alignment step.

C. Deterministic fabrication of the cavities

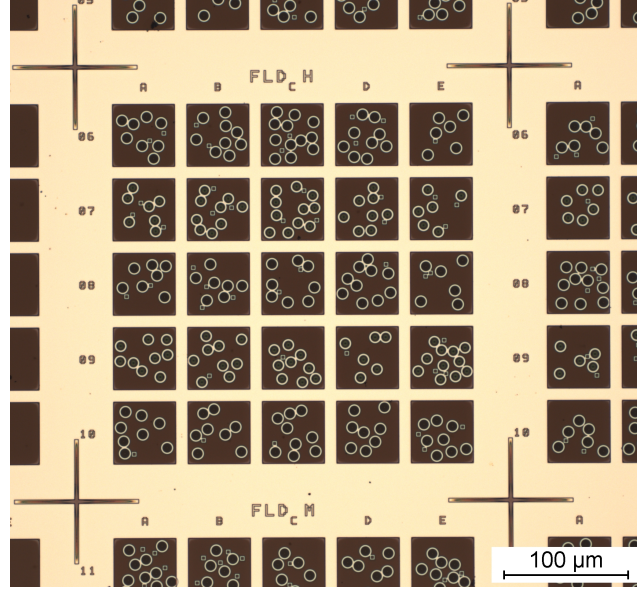
After determining the positions of QDs with respect to the AMs, we continue the deterministic workflow by the nanofabrication of the cavities. We deposit a 110 nm-thick SiN_x layer in PECVD on top of the InP membrane as a hard-mask and spin-coat CSAR e-beam resist on top of it. We expose the resist by the EBL, using the AMs outside the imaging fields in the form of InP crosses remaining on SiO_2 . We develop the resist and transfer the cavities to the SiN_x hard-mask by employing ICP-RIE with SF_6 -based etch recipe. Residual CSAR is stripped in Remover 1165 followed by 10 min descum in the barrel-type plasma asher. Subsequently, the pattern is transferred into the InP layer in ICP-RIE by HBr-based etch.

Supplementary Fig. S4 shows the optical microscope image of the sample's surface taken at $20\times$ magnification with the cavities transferred to InP. The imaged fragment of the chip shows a 5×5 pattern of the imaging fields with four InP crosses at the corners of the pattern. Also visible are additional, 2 μm side-length square mesas.

S-III. ACCURACY OF DETERMINATION OF QD POSITIONS FROM μPL MAPS AND FINAL CAVITY POSITIONING

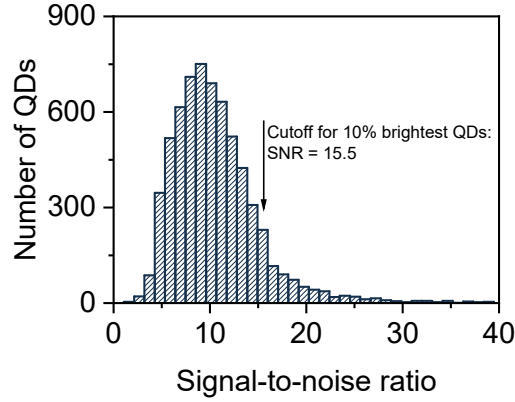
A. Signal-to-noise ratio

Supplementary Fig. S5 shows the histogram of signal-to-noise ratio (SNR) for the mapped QDs. The average SNR is 10.6 which underlines the crucial role of the 7-fold enhancement of the signal intensity for the planar structure by application of the



Supplementary Fig. S4. The optical microscope image of the sample's surface taken at 20 \times magnification with the cavities transferred to InP.

metallic mirror [7]. Based on this result, we deduce that for a sample without such a mirror, the SNR would be roughly 7 times lower (SNR of about 1.5), which would make the optical localization of QDs impossible (compare with the noise level in Figs. 2e and 2f in the main text).



Supplementary Fig. S5. Histogram of signal-to-noise ratio for the recorded QD spots.

B. Localization algorithm

Our algorithm calculates the scaling factor P [px/ μ m] to change the map unit from pixels (px) to μ m. For a given μ PL map, we identify n QD spots and take $2n$ cross-sections of the map (each QD is sectioned in two directions). The width of each cross-section is taken to equal a few pixels centered at the QD spot maximum to increase the signal-to-noise ratio (SNR). We found the best SNR for 10 pixels and used this value consistently.

For the i -th cross-section, we determine the positions $\mathbb{M}_{i,l}$ [px], $\mathbb{M}_{i,u}$ [px]¹ of the field boundaries (acting as reference/alignment marks, AMs; indices l and u stand for lower and upper field boundaries, the same indices are applied also for left and right field

¹ For clarity, we use the blackboard-bold font for quantities given in pixels, e.g. \mathbb{M} , \mathbb{Q} . The normal font is used for the same dimensions given in μ m, e.g. Q .

edges) and Q_i [px] for the QD spot position. All values $M_{i,l}$, $M_{i,u}$, and Q_i are the centers of the Gaussian peaks, fitted to respective maxima on the μ PL map cross-section. Additionally, we assume that each field is a square of size $F = 50 \mu\text{m}$.

P is calculated by averaging over all cross-section-related coefficients P_i recorded for a given field ($P = \bar{P}_i$) to ensure its highest accuracy, according to the formula

$$P = \frac{1}{2n} \sum_{i=1}^{2n} P_i = \frac{1}{2n} \sum_{i=1}^{2n} \frac{|M_{i,u} - M_{i,l}|}{F}. \quad (\text{S8})$$

Calculating P separately for each map accounts for possible slight changes in the magnification due to defocusing of the sample surface during the cryostat translation, however, we find very low dispersion of P coefficients for different μ PL maps (see the following section and Supplementary Fig. S6).

Then, the i -th QD position Q_i [μm] (vertical or horizontal) is calculated as

$$Q_i = \frac{Q_i - M_{i,l}}{P}. \quad (\text{S9})$$

C. Uncertainty of scaling the μ PL maps

The accuracy of the scaling factor ΔP_i for a single (i -th) μ PL map cross-section can be calculated by propagating the uncertainties in Eq. (S8):

$$\Delta P_i = \sqrt{\left(\frac{\Delta M_{i,u}}{F}\right)^2 + \left(\frac{\Delta M_{i,l}}{F}\right)^2 + \left(\frac{\Delta F}{F^2}\right)^2}.$$

The uncertainty of the field size ΔF has two contributions, the uncertainty of the electron beam lithography alignment, estimated to $\Delta C = 40 \text{ nm}$ [8] and the over-etching Δx during the ICP-RIE step (estimated to be up to $\Delta x = 40 \text{ nm}$), potentially influencing F by $2\Delta x = 80 \text{ nm}$. $\Delta M_{i,u}$ and $\Delta M_{i,l}$ are standard errors of the numerical fitting.

However, to increase the accuracy of the determination of the scaling factor, we average the P_i values for all cross-sections taken in a particular μ PL map, as can be seen in Eq. (S8), so as the uncertainty ΔP we adopt the estimator of the standard error of mean $\hat{\sigma}_{\bar{P}}$ for the sample defined as a set of all $2n$ factors $P_i = |M_{i,u} - M_{i,l}|/F$ determined for a given μ PL map:

$$\Delta P = \hat{\sigma}_{\bar{P}} = \frac{\sigma_{P_i}}{\sqrt{2n}}, \quad (\text{S10})$$

where σ_{P_i} is the sample standard deviation.

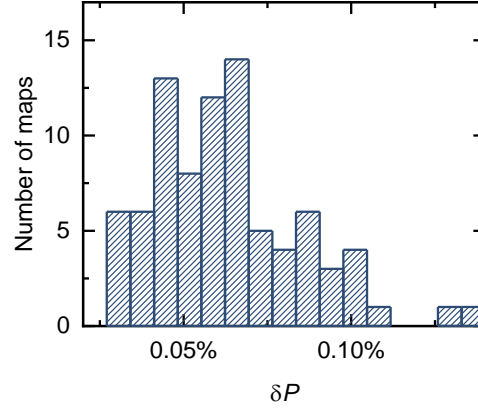
According to calculated statistics for $m = 84$ exemplary μ PL maps, we can compare the estimators of the standard error of mean $\hat{\sigma}_{\bar{P}}$ determined separately for each μ PL map and reach the following conclusions:

1. We find that the coefficients P_i are very close to each other, evidencing no perceptible elongation or distortion of the registered images. This can be evaluated by the analysis of the set of calculated (for all m maps) uncertainties $\Delta P = \hat{\sigma}_{\bar{P}}$ scaled by the determined P factors: $\delta P = \Delta P/P$. We plot the histogram of δP in Supplementary Fig. S6 and find the median value of δP -distribution of 0.06%. In other words, for half of the analyzed maps, the distribution of P_i factors is sufficiently narrow to determine the P factor with relative uncertainty $\delta P < 0.06\%$. This value includes the potential elongation of the image (difference in vertically and horizontally determined P_i factors).
2. The stability of the setup and overall repetitiveness of the imaging process is high as the image magnification varies very little between maps. This can be evaluated by the estimator of the standard error of mean $\hat{\sigma}_{\bar{P}}$ calculated not for different cross-sections [averaging P_i values for a given map, as in Eq. (S8)] but for different maps (averaging P values for all maps). We obtain $\hat{\sigma}_{\bar{P}}/\bar{P} = 0.013\%$. We take this value as the estimation of variation of the setup magnification during the imaging process.

Then, the accuracy of cavity positioning ΔR depends primarily on the accuracy of the QD localization (ΔQ) and EBL alignment uncertainty ΔC . The ΔQ itself depends on the fit standard errors (ΔM , ΔQ), and scaling factor uncertainty ΔP .

D. Image rotation ϕ

Although we carefully align the image of the field with the horizontal and vertical axes of the detector array, we assume that there can be some indiscernible rotation of the image ϕ on the level of up to a few degrees. Even if this is the case, the rotation



Supplementary Fig. S6. The histogram of relative μPL map scaling uncertainty $\delta P = \Delta P / P$ for the set of analyzed $m = 84$ exemplary μPL maps.

results first in the larger separation between AM peaks in the cross-sections ($|\mathbb{M}_{i,u} - \mathbb{M}_{i,l}| / \cos \varphi$ instead of $|\mathbb{M}_{i,u} - \mathbb{M}_{i,l}|$) and this is translated to scaled P : $P \rightarrow P / \cos \varphi$, according to Eq. (S8). The distance between lower AM and QD is however also elongated, $(Q_i - \mathbb{M}_{i,l}) / \cos \varphi$ instead of $(Q_i - \mathbb{M}_{i,l})$. According to Eq. (S9), the new QD position is:

$$Q_{i,\text{new}} = \frac{(Q_i - \mathbb{M}_{i,l}) / \cos \varphi}{P / \cos \varphi} = Q_i,$$

so that the slight image rotation has no influence on the determination of QD position Q_i in our approach.

E. One-dimensional QD position ΔQ_i

The determination of i -th QD position Q_i is influenced by the scaling factor uncertainty ΔP , as well as QD (ΔQ_i) and lower AM ($\Delta \mathbb{M}_{i,l}$) fit uncertainties (standard errors of the numerical fitting), and is calculated by propagating the uncertainties, according to Eq. (S9):

$$\Delta Q_i = \sqrt{\left(\frac{\Delta Q_i}{P}\right)^2 + \left(\frac{\Delta \mathbb{M}_{i,l}}{P}\right)^2 + \left(\frac{(Q_i - \mathbb{M}_{i,l}) \Delta P}{P^2}\right)^2}. \quad (\text{S11})$$

F. Two-dimensional QD position ΔQ

We combine the one-dimensional QD position uncertainties ΔQ_i into the two-dimensional uncertainty using the formula

$$\Delta Q = \sqrt{(\Delta Q_h)^2 + (\Delta Q_v)^2}, \quad (\text{S12})$$

where $\Delta Q_h, \Delta Q_v$ are ΔQ_i values calculated according to Eq. (S11) for horizontal and vertical cross-sections. We use the ΔQ value to determine the accuracy of our μPL imaging method.

G. Distance between QD position and cavity center R – accuracy of cavity positioning ΔR

We express the uncertainty ΔR of the expected distance $R = 0$ between the QD position and the cavity center as

$$\Delta R = \sqrt{(\Delta Q)^2 + (\Delta C)^2}. \quad (\text{S13})$$

H. Example calculations for QD-CBGs #1–#3

Finally, in Supplementary Tab. **S1** we show the uncertainties involved in the determination of the QD position ΔQ_i accordingly to Eq. (S11) and of the accuracy of cavity positioning ΔR accordingly to Eq. (S13) for three exemplary QD-CBGs #1–#3, described in the article (QD-CBG #1 and QD-CBG #2) and in the following part of the **Supplemental Material** (QD-CBG #3).

Supplementary Table S1. Uncertainties involved in the determination of accuracy of cavity positioning ΔR for exemplary devices QD-CBGs #1–#3.

Device	Orientation	$\Delta Q_i/P$	$\Delta M_i/P$	$(Q_i - M_{i,l}) \Delta P/P^2$	ΔQ_i	ΔQ	ΔR
QD-CBG #1	Vertical	61.0 nm	14.4 nm	19.9 nm	65.8 nm	141.9 nm	147.4 nm
	Horizontal	120.0 nm	29.0 nm	23.5 nm	125.7 nm		
QD-CBG #2	Vertical	61.9 nm	12.7 nm	20.1 nm	66.3 nm	137.3 nm	143.0 nm
	Horizontal	115.7 nm	26.1 nm	20.2 nm	120.2 nm		
QD-CBG #3	Vertical	112.2 nm	20.7 nm	12.0 nm	114.7 nm	132.9 nm	138.8 nm
	Horizontal	59.5 nm	19.5 nm	24.6 nm	67.2 nm		

I. Calculation of the diffraction-limited spot size

In this and the following subsections, we consider a QD as a point light source and calculate the expected observed width of such a source in our imaging setup shown in Fig. 2a of the main text. Its emission can be described by the point spread function (PSF) of the setup, which for the approximation of 2D paraxial wide-field fluorescence microscope forms an Airy disc (first-order Bessel function of the first kind) [9].

Our QD localization algorithm uses the approximation of the Bessel function by the Gaussian profile, which we use for fitting the QD- and AM-related signal in the cross-sections of μ PL maps.

First, we calculate the standard deviation σ_{diff} of the Gaussian curve that best approximates the PSF of our setup according to the formula [9]:

$$\sigma_{\text{diff}} \approx 0.21 \frac{\lambda_{\text{QD}}}{\text{NA}} = 0.501 \mu\text{m} \quad (\text{S14})$$

with employed $\text{NA} = 0.65$ and $\lambda_{\text{QD}} = 1.55 \mu\text{m}$. Then, we translate σ_{diff} to full width at half-maximum (FWHM) as

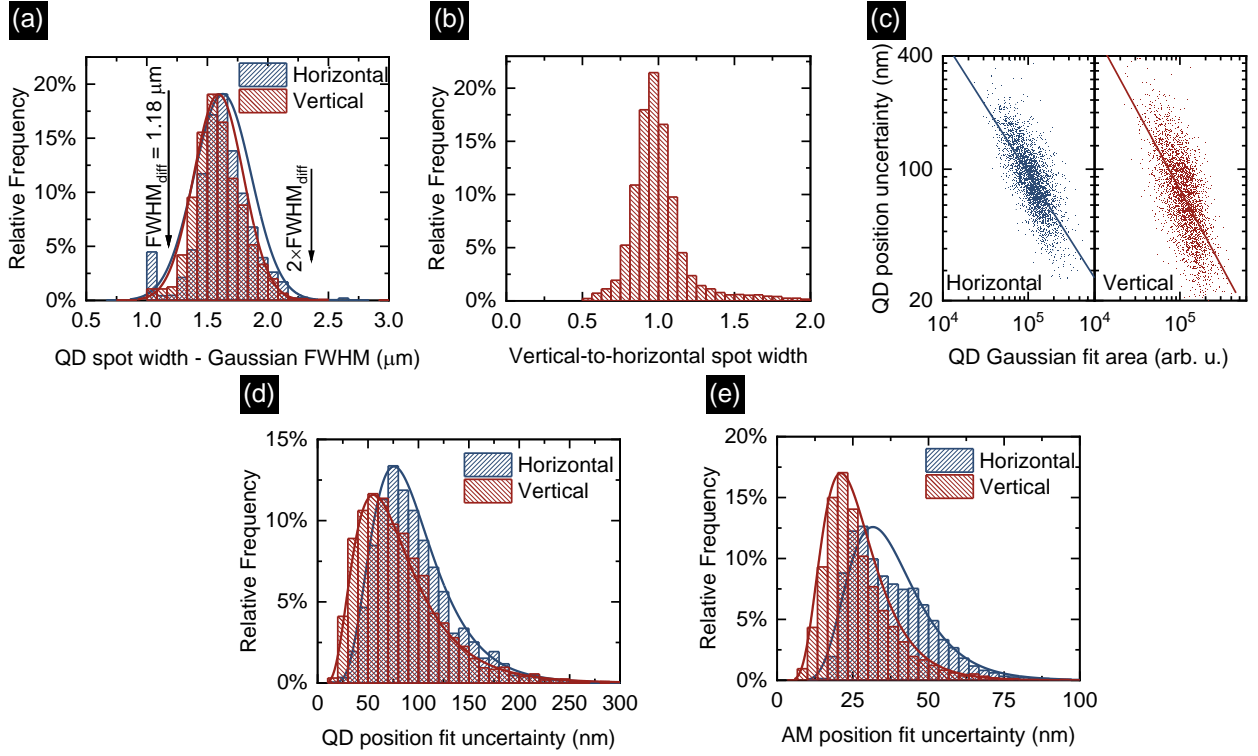
$$\text{FWHM}_{\text{diff}} = 2\sqrt{2 \ln 2} \times \sigma_{\text{diff}} \approx 1.18 \mu\text{m}. \quad (\text{S15})$$

J. Statistics on QD spot size and the accuracy of QD positioning

We take the calculated $\text{FWHM}_{\text{diff}} = 1.18 \mu\text{m}$ (see previous section) as the diffraction-limited spot size and compare it with the histogram of all FWHM values for registered QD spots in Supplementary Fig. **S7a**. The medians for the registered FWHM values are similar for horizontal and vertical cross-sections, $1.62 \mu\text{m}$ and $1.58 \mu\text{m}$, respectively, which is $\sim 35\%$ more than the calculated $\text{FWHM}_{\text{diff}}$. Almost all registered FWHM values are lower than $2 \times \text{FWHM}_{\text{diff}}$. Therefore, our imaging setup operates close to the diffraction limit with residual broadening originating most probably from the cryostat window between the QDs and microscope objective [10]. The similarity between horizontal and vertical spot widths is evidenced by the histograms of ratios between the widths of the fitted horizontal and vertical cross-sections of the QD Gaussian profiles ("Vertical-to-horizontal spot width"), presented in Fig. **S7b**. The average ratio is determined as 99.78% , in other words, it differs only by 0.22% from the ideal case unity ratio. The standard sample deviation for the ratio values distribution is calculated to be $\sigma = 19.24\%$.

As expected, the fitting uncertainty $\Delta Q_i/P$ is correlated with the QD brightness, here estimated by the Gaussian fit area, and the corresponding plot is shown in Supplementary Fig. **S7c**. We find a strong negative correlation between considered fit parameters (Pearson correlation coefficient of -0.68 and -0.73 for horizontal and vertical cross-sections, respectively).

Supplementary Figure **S7d** presents the fitting uncertainty for QD positions $\Delta Q_i/P$, separately for horizontal and vertical cross-sections. The uncertainty is defined as the standard error of the fitting procedure for estimation of the center of the Gaussian profile and in all analyzed cases, the obtained values form positively skewed distributions that follow the log-normal distribution,



Supplementary Fig. S7. Parameters of fitting the μ PL map cross-sections, shown separately for horizontal and vertical directions. **a**, the histogram of FWHM values for the fits used for the determination of QD position Q compared with the calculated diffraction-limited value $\text{FWHM}_{\text{diff}} = 1.18 \mu\text{m}$ [Eq. (S15)] and fitted with the normal distribution curves, **b**, histogram of the ratio between the widths of the fitted horizontal and vertical cross-sections of the QD Gaussian profiles, based on the panel (a), **c**, QD position fit uncertainty $\Delta Q_i/P$ as a function of the QD fit area, **d**, histogram of the QD position fit uncertainty $\Delta Q_i/P$, **e**, AM position fit uncertainty $\Delta M_i/P$. Histograms in panels (d) and (e) are fitted with log-normal distributions.

as shown with fit curves. The medians for $\Delta Q_i/P$ are 88.6 nm and 73.6 nm for horizontal and vertical cross-sections, with 24 % of vertical uncertainties being below 50 nm.

Finally, we analyze the fitting uncertainty for AMs positions $\Delta M_i/P$, as it influences the uncertainty of QD position ΔQ_i determination via Eq. (S11). The medians for $\Delta M_i/P$ distributions, shown in Supplementary Fig. S7e, are 24.1 nm and 35.1 nm for horizontal and vertical cross-sections. Importantly, 83 % of horizontal and 95 % of vertical cross-section uncertainties $\Delta M_i/P$ are below 50 nm.

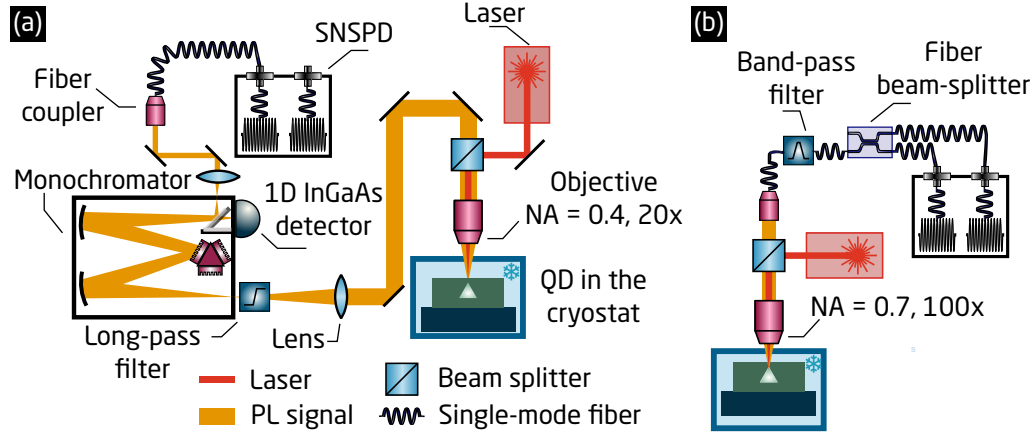
Based on these considerations and the correlation between QD spot brightness and uncertainty of QD position fit $\Delta Q_i/P$, we estimate that working with only the brightest QD spot in each imaging field (due to the average number of $N_F \approx 10$ spots detected per field, this amounts to limiting cavity fabrication to 10 % of the registered spots), our fitting accuracy would be $\Delta Q_i/P < 53.2$ nm and $\Delta Q_i/P < 37$ nm for horizontal and vertical cross-sections (10th percentiles for the uncertainties distributions). Taking medians for the fitting uncertainty of AMs positions $\Delta M_i/P$, we find the uncertainty of QD localization $\Delta Q < 80.1$ nm, cf. Eq. (S12). Including the electron beam lithography uncertainty $\Delta C = 40$ nm, we find the total uncertainty of cavity placement $\Delta R < 90.3$ nm, according to Eq. (S13) (see Supplementary Tab. S2). Here, we assume $(Q_i - M_{i,l}) = 25 \mu\text{m}$ (center of the field) and for ΔP we take the median value of standard error of mean $\hat{\sigma}_{\bar{P}}$ calculated for 84 exemplary μ PL maps.

Supplementary Table S2. Uncertainties involved in the determination of the accuracy of cavity positioning ΔR for an example of a QD with low uncertainty of fitting the QD positions $\Delta Q_i/P$ – corresponding to a QD being in the 10 % of the brightest spots.

Orientation	$\Delta Q_i/P$	$\Delta M_i/P$	$(Q_i - M_{i,l}) \Delta P / P^2$	ΔQ_i	ΔQ	ΔR
Horizontal	≤ 53.2 nm	24.1 nm	15.1 nm	< 61.1 nm	< 80.1 nm	< 90.3 nm
Vertical	≤ 37 nm	35.1 nm		< 53.2 nm		

S-IV. OPTICAL SETUPS

Supplementary Fig. S8a presents the setup used for spectroscopy studies of fabricated devices (μ PL, extraction efficiency determination, time-resolved μ PL), while the above-band autocorrelation histograms are recorded in a setup shown in Supplementary Fig. S8b. Details of the equipment used are given in the **Methods** section.



Supplementary Fig. S8. Simplified schemes of the experimental setups used for the device characterization. **a**, the optical setup used for the determination of the photon extraction efficiency and time-resolved μ PL, **b**, setup used for autocorrelation experiments. SNSPD – superconducting nanowire single-photon detector.

S-V. DETERMINATION OF THE PHOTON EXTRACTION EFFICIENCY

To determine the value of photon extraction efficiency η , we calibrate the optical setup shown in Supplementary Fig. S8a and calculate its efficiency η_{Setup} as a multiplication of the transmission of all optical elements and of the efficiency of fiber in-coupling and superconducting nanowire single-photon detector (SNSPD) quantum efficiency. We start with reflecting the laser tuned to $1.55\mu\text{m}$ off a silver mirror placed in the setup instead of the structure. The signal emitted from the sample passes through the elements enumerated in Supplementary Tab. S3, given with their measured transmission efficiencies. For SNSPD, we take nominal efficiency. We obtain $\eta_{\text{Setup}} = (1.10 \pm 0.17)\%$, where the uncertainty is calculated by propagating the assumed uncertainties of transmission of the consecutive elements.

Supplementary Table S3. The transmission of the optical components in the setup used for determination of photon extraction efficiency, as shown in Supplementary Fig. S8a.

Element	Transmission/Efficiency
cryostat window	$(90 \pm 2)\%$
microscope objective	$(55 \pm 3)\%$
beam splitter	$(38 \pm 2)\%$
a set of mirrors	$(85 \pm 5)\%$
focusing lens and long-pass filter	$(93 \pm 2)\%$
monochromator	$(27 \pm 5)\%$
mirrors for signal coupling	$(96 \pm 2)\%$
fiber in-coupling	$(41 \pm 10)\%$
fibers and their connections	$(80 \pm 10)\%$
SNSPD efficiency	$(87 \pm 3)\%$
Total setup efficiency η_{Setup}	$(1.10 \pm 0.17)\%$

Then, we excite the QDs off-resonantly with a pulsed laser diode with $f_{\text{rep}} = 80 \text{ MHz}$ repetition rate at the saturation power for each QD. We collect the emission with the microscope objective ($\text{NA} = 0.4$) and take the SNSPD count rate n_{QD} for the most intense QD lines, and correct them by η_{Setup} and f_{rep} according to the formula

$$\eta = \frac{n_{\text{QD}}}{f_{\text{rep}} \times \eta_{\text{Setup}}}. \quad (\text{S16})$$

The uncertainty of the photon extraction efficiency for QD-CBG #1 and #2 are calculated by propagating the uncertainties as

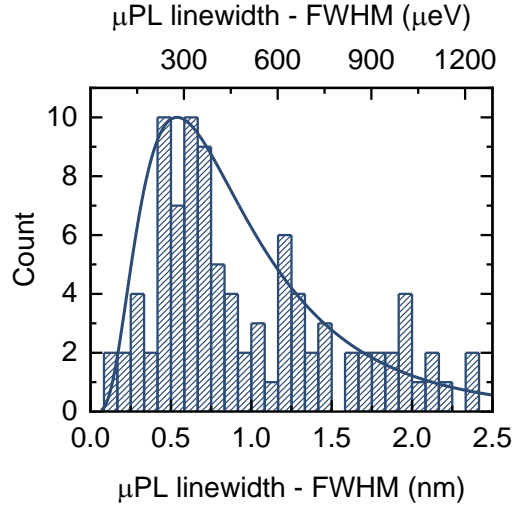
$$\Delta\eta = \sqrt{\left(\frac{\Delta n_{\text{QD}}}{\eta_{\text{Setup}}}\right)^2 + \left(\frac{n_{\text{QD}} \Delta\eta_{\text{Setup}}}{\eta_{\text{Setup}}^2}\right)^2}, \quad (\text{S17})$$

with $\Delta n_{\text{QD}} = 1000$ and $\Delta\eta_{\text{Setup}} = 0.17\%$. This method assumes unity internal quantum efficiency of QDs ($\eta_{\text{int}} = 100\%$), so that the QD photon emission rate equals f_{rep} . It is however difficult to determine experimentally the contribution of non-radiative recombination and hence the real value of η_{int} . The assumption of $\eta_{\text{int}} = 100\%$ thus sets a lower limit of η due to a possible overestimation of the total number of photons emitted by the QD.

S-VI. SUPPORTING μPL DATA FOR QD-CBG DEVICES

A. QD linewidths

Supplementary Figure S9 presents the histogram of linewidths for all 102 found QDs emitting in the CBGs. We use the FWHM of the fitted Gaussian profiles to describe the linewidth and find that the median linewidth is 0.76 nm, 1st quartile 0.52 nm, and the minimal value 0.14 nm. Additionally, the linewidths for QD-CBGs #1–#3 are shown in Supplementary Tab. S4.

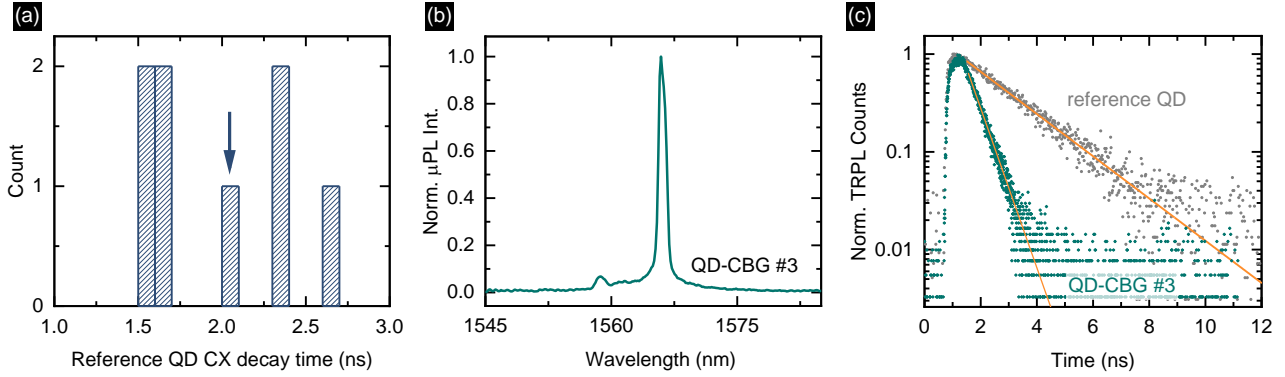


Supplementary Fig. S9. The histogram of linewidths for QDs in CBGs (FWHM of fitted Gaussian profiles).

Supplementary Table S4. μPL linewidths of QD-CBGs #1–#3.

QD	QD linewidth in μPL
QD-CBG #1	0.47 nm
QD-CBG #2	0.17 nm
QD-CBG #3	0.19 nm

B. Time-resolved μ PL



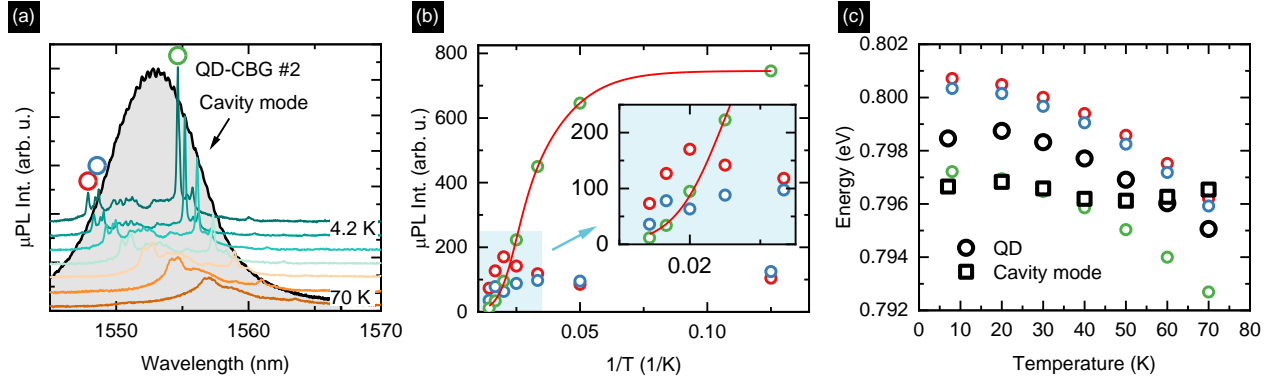
Supplementary Fig. S10. Additional μ PL data. **a**, Histogram of recorded decay times for reference QD trion lines; arrow points to the QD shown in Fig. 3b in the article and in panel (c), **b**, μ PL spectrum for QD-CBG #3, **c**, time-resolved μ PL time traces for QD-CBG #3 and the reference QD.

Supplementary Figure S10 shows the μ PL data supporting the determination of F_P . We focus on an additional QD-CBG #3 with a well-isolated transition line, analogous to QD-CBGs #1 and #2 presented in the article, Fig. 3.

Fig. S10a shows a histogram of recorded decay times for the reference QD trion lines. The time-resolved μ PL results for eight QDs found in the area outside the fabricated cavities with intense trion lines indicate a considerable scattering of the decay times, with minimal and maximal registered times 1.59 ns and 2.69 ns and the average decay time $\tau_{\text{ref}} = 1.99$ ns. The standard deviation of the fitted normal distribution is 0.44 ns and the standard error of mean is 0.16 ns. We take the average decay time $\tau_{\text{ref}} = (1.99 \pm 0.16)$ ns to calculate the F_P according to formula $F_P = \tau_{\text{ref}} / \tau_{\text{cav}}$.

Fig. S10b shows the spectrum of QD-CBG #3, and Fig. S10c presents time-resolved μ PL decay traces in analogy to Fig. 3b of the article, where the same reference time trace is presented. Decay time for QD-CBG #3 is the same as for QD-CBG #2 within the fitting accuracy, $\tau_{\#3} = \tau_{\#2} = (0.53 \pm 0.01)$ ns, what translates to $F_P = 3.75 \pm 0.30$.

C. Temperature-dependent μ PL



Supplementary Fig. S11. Analysis of the temperature-dependent μ PL spectra for QD-CBG #2. **a**, Temperature-dependent μ PL spectra for QD-CBG #2, overlapped with the cavity mode. **b**, Arrhenius plot for the integrated μ PL intensity for three QD lines, indicated with the same symbols in panel (a). Inset: close-up of the marked region. **c**, μ PL emission energy for the same QD lines. Black symbols stand for another QD-CBG device, with QD and cavity mode energies tracked up to $T = 70$ K. The mode crossing characteristic for the weak QD-cavity coupling regime is visible.

We record the temperature-dependent μ PL signal for QD-CBG #2 in the temperature range of $T = 4.2\text{ K}$ to 70 K under the continuous-wave (cw) excitation and present the stacked spectra in Fig. S11a. Three emission lines, marked with rings, can be identified and their emission intensity and energy tracked as the temperature is increased. We plot also the mode profile for reference. Note the $\sim 2\text{ nm}$ redshift of the most intense line from the central wavelength of the cavity.

The μ PL intensities change differently for lines with emission energy lower vs. higher compared to the mode profile. The short-wavelength lines, marked with red and blue rings, are tuned across the mode profile as the temperature raises. Their μ PL intensity quench is greatly suppressed, in fact, the intensity of the line marked with a red circle has a maximum at $T = 50\text{ K}$. The behavior for the long-wavelength line, marked with a green ring, is opposite and its intensity quenches fast.

The temperature-dependent μ PL intensity for the most intense line marked with the green ring is fitted with a standard formula assuming two activation processes [11]:

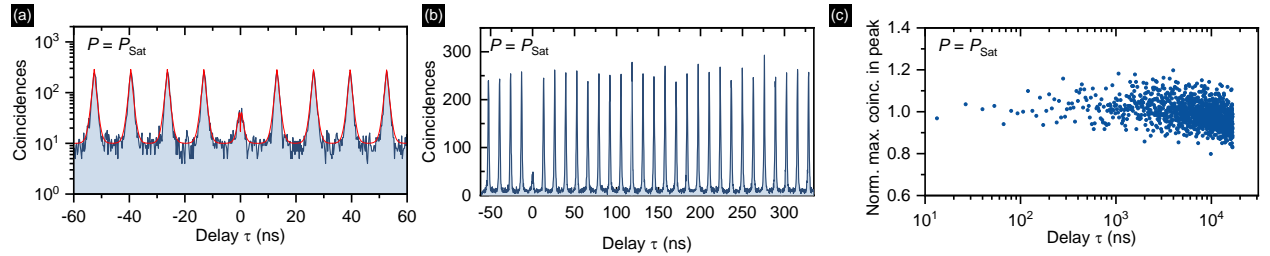
$$I(T) = \frac{I_0}{1 + B_1 \exp(-E_{a,1}/k_B T) + B_2 \exp(-E_{a,2}/k_B T)}, \quad (\text{S18})$$

where I_0 is the μ PL intensity for $T \rightarrow 0$, $E_{a,1}$ and $E_{a,2}$ are activation energies, and B_1 and B_2 are relative rates corresponding to the efficiency of involved processes. We achieve the activation energies of $E_{a,1} = (6.9 \pm 0.8)\text{ meV}$ and $E_{a,2} = (27.9 \pm 3.1)\text{ meV}$. We note that $E_{a,2}$ is similar to the activation energy $E_{\text{Ref}} = (23.6 \pm 0.8)\text{ meV}$ found for a CX line from analogous QDs [7]. Accordingly to Ref. [12], this activation energy can be attributed to the charge transfer to higher orbital states, based on the band structure calculations within the 8-band $k \cdot p$ framework. Hence, another mechanism is responsible for the identification of $E_{a,1}$ energy which is absent in the case of high-energy lines (blue and red circles, see Supplementary Fig. S11b). This can potentially be associated with the enhancement of the QD emission rate when the overlap between the line and the mode energy is maximized.

In Supplementary Figure S11c we plot the temperature dependence of the emission energy for lines analyzed in Supplementary Fig. S11b and, additionally, for another investigated QD-CBG device, where the observation of the crossing of the temperature-tuned QD line and the cavity mode under high power off-resonant cw excitation was possible due to the QD energy being higher than the mode energy at $T = 4.2\text{ K}$. The temperature-induced evolution of cavity mode energy (black open squares) can be compared with the QD lines, evidencing a weaker temperature dependence, as expected for the cavity mode.

S-VII. QUANTUM OPTICS EXPERIMENTS

A. Off-resonant autocorrelation data for QD-CBG #2



Supplementary Fig. S12. Analysis of the second-order autocorrelation function $g^{(2)}(\tau)$ of the photons emitted from QD-CBG #2 under pulsed off-resonant excitation for laser excitation power P corresponding to saturation of the CX line. **a**, **b**, The recorded histogram **c**, Normalized maximum number of coincidences for all 1260 registered peaks for positive delays of histogram shown in (b).

Supplementary Figure S12 shows the autocorrelation histogram recorded under pulsed off-resonant excitation for QD-CBG #2. We do not observe blinking there, as the normalized coincidences in consecutive peaks (maximum number of coincidences without fitting) in the $g^{(2)}(\tau)$ histogram is at a constant level (Supplementary Fig. S12c). We show data for all registered 1260 peaks, i.e. up to $\tau = 16.7\mu\text{s}$ delay. Fluctuation in the data originates in the discretization of the $g^{(2)}(\tau)$ due to finite time binning in the experiment. The blinking would indicate the occupation of a meta-stable QD state [13], originating, e.g., in the emission wavelength fluctuations due to nearby defects [14] or trapped charges [15].

We fit the histograms with the function [16, 17]:

$$C(\tau) = B + A [\exp(-|\tau|/\tau_{\text{dec}}) - \exp(-|\tau|/\tau_{\text{cap}})] + H \sum_{n \neq 0} \exp(-|\tau - n\tau_0|/\tau_{\text{dec}}), \quad (\text{S19})$$

where B is the level of background coincidences, A is a scaling parameter related to secondary photon emission, $n \neq 0$ is the peak number, τ_0 is the laser pulse period, and H the average height of the peaks at $\tau_n = n\tau_0$. The second-order correlation function $g^{(2)}(\tau)$ is then obtained by normalizing $C(\tau)$ with $(H + B)$.

The time-independent level of background coincidences B originates from the detector dark counts and uncorrelated photons contributing to the registered histograms. Our approach allows taking into account only coincidences caused by the QD signal. We define the purity as the ratio between the QD emission coincidences registered at τ_0 peak (area of this peak) to the average number of coincidences (peak area) registered at $\tau_{n \neq 0}$ peaks. Then, the $g^{(2)}(0)$ value is calculated by first subtracting the background contribution B , integrating the areas under the central peak and under the non-zero peaks, and dividing these two integrals, according to the formula:

$$g^{(2)}(0)_{\text{fit}} = \frac{\int_{-\tau_0/2}^{\tau_0/2} A [\exp(-|\tau|/\tau_{\text{dec}}) - \exp(-|\tau|/\tau_{\text{cap}})] d\tau}{\int_{-\tau_0/2}^{\tau_0/2} H \exp(-|\tau|/\tau_{\text{dec}}) d\tau}. \quad (\text{S20})$$

Supplementary Table. S5 summarizes the fit parameters for off-resonant autocorrelation histograms obtained for $0.5 \times P_{\text{sat}}$ and P_{sat} excitation power. The uncertainties are determined from the fit uncertainties and propagated in the case of $g^{(2)}(0)_{\text{fit}}$ which is calculated from the fit parameters.

Supplementary Table S5. Fitting parameters for off-resonant autocorrelation measurement.

Fit parameter	Off-resonant excitation power	
	$0.5 \times P_{\text{sat}}$	P_{sat}
Background contribution, B	14.4 ± 2.0	10.2 ± 0.7
Scaling of the center peak, A	54 ± 15	67 ± 19
Height of $\tau_{n \neq 0}$ peaks, H	187 ± 10	288 ± 3
Laser period, τ_0	$(13.15 \pm 0.01) \text{ ns}$	$(13.14 \pm 0.01) \text{ ns}$
Decay time, τ_{dec}	$(678 \pm 5) \text{ ps}$	$(721 \pm 10) \text{ ps}$
Recapture time, τ_{cap}	$(544 \pm 76) \text{ ps}$	$(196 \pm 98) \text{ ps}$
$g^{(2)}(0)_{\text{fit}}$, Eq. (S20)	0.05 ± 0.02	0.17 ± 0.03

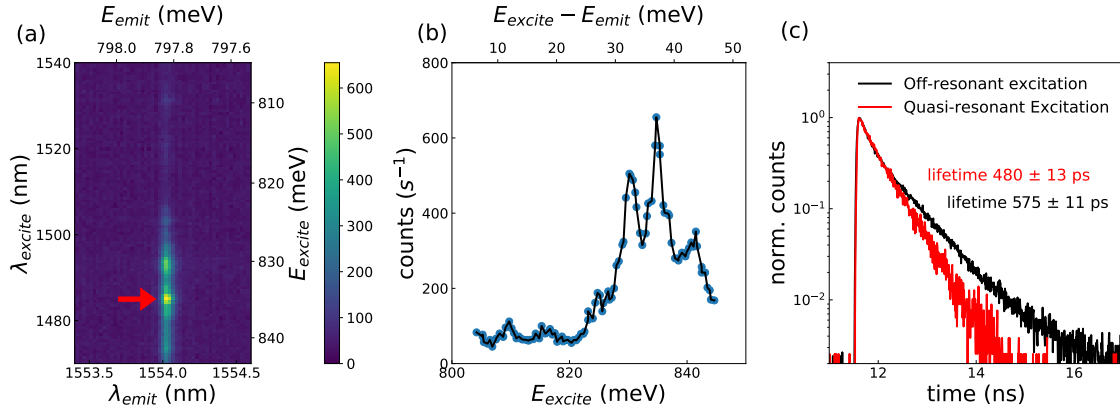
B. Microphotoluminescence excitation spectroscopy of QD-CBG #2

The two-photon interference experiments were carried out under quasi-resonant excitation conditions. The exact excitation energy was determined based on the microphotoluminescence excitation (μPLE) experiment conducted with a pulsed tunable laser with 5 ps-long pulses and 80 MHz repetition rate. The excitation laser wavelength was varied in the range of 1470-1540 nm at constant average excitation power of $25 \mu\text{W}$ measured in front of the cryostat window. In the μPLE map, shown in Supplementary Fig. S13a, a clear maximum is visible at the wavelength 1484.2 nm, corresponding to 835.37 meV photon energy which was used for all experiments described in this section. The energy difference of 37.57 meV (see the map cross-section in Supplementary Fig. S13b) coincides reasonably well with the LO phonon energy of InP of 43.4 meV at low temperature [18]. Simultaneously, the measured energy difference is far above the calculated trion p -shell splitting of about $\sim 20 \text{ meV}$ [12] for QDs very similar in size and chemical composition (P admixture) to the ones investigated here. Therefore, we assume that the applied quasi-resonant excitation of the QD is LO-phonon-assisted.

The comparison of the time-resolved μPL time traces for the trion line in QD-CBG #2 for quasi- and off-resonant excitation, shown in Supplementary Fig. S13c, confirms the accelerated relaxation of the excited state by the reduced decay time under for the quasi-resonant excitation.

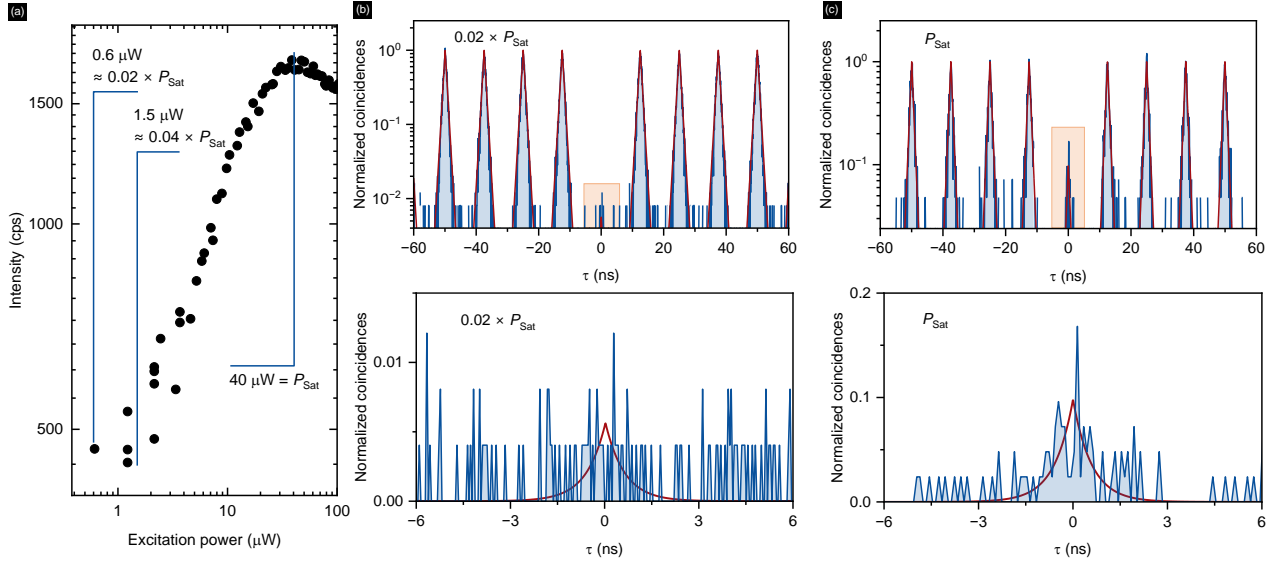
C. Quasi-resonant autocorrelation data for QD-CBG #2

The single-photon purity was verified in autocorrelation measurements taken at various excitation powers to identify the contribution of multi-photon emission and unsuppressed reflected laser light which lead to erroneous coincidences in HOM measurements. The lowest $g^{(2)}(0)$ value was found for the excitation power of $1.5 \mu\text{W}$, and the corresponding autocorrelation data is shown in Fig. 4a of the main text. In this configuration, the autocorrelation histogram was measured directly through the HOM setup to make sure that no reflected laser obscures the HOM experiment. Increasing the excitation power is favored by



Supplementary Fig. S13. **a**, Microphotoluminescence excitation map of QD-CBG #2. **b**, Cross-section of the map taken at the center of the QD-CBG #2 emission line, revealing the quasi-resonant excitation energy of ~ 0.835 eV used to excite the QD for the indistinguishability measurements. The energy difference corresponds to the detuning of ~ 37 meV from the emission energy. **c**, Time-resolved μ PL data for line in QD-CBG #2 for quasi- and off-resonant excitation.

increasing the signal-to-background ratio as long as the QD is in the linear response regime. On the other hand, increasing the excitation power once the QD emission intensity is saturated results mostly in the increase of the background counts due to the cavity being fed by other sources. They mostly originate in the low-energy tail of the wetting layer emission or radiative defects present in the sample.



Supplementary Fig. S14. **a**, Excitation-power dependent μ PL intensity of the line in QD-CBG #2 under quasi-resonant excitation with the powers chosen for HOM measurements marked. **b**, **c**, Autocorrelation histograms for QD-CBG #2 under (b) $P_{exc} = 0.6 \mu$ W ($0.02 \times P_{Sat}$), (c) $P_{exc} = 40 \mu$ W (P_{Sat}). Orange boxes mark the region that is zoomed in at the bottom.

The low power autocorrelation measurement taken using the HOM configuration leads to an integrated $g^{(2)}(0)_{raw} = (3.2 \pm 0.6) \times 10^{-3}$ which confirms the suppression of the excitation laser in preparation for the HOM experiment.

To fit the autocorrelation histograms we modify Eq. (S19) used for fitting off-resonant data, as we do not observe background

counts ($B = 0$) and no carrier recapture so that the new formula reads

$$C(\tau) = c \cdot \left(g^{(2)}(0)_{\text{fit}} \exp(-|\tau|/\tau_{\text{dec}}) + \sum_{n \neq 0} \exp(-|\tau - n\tau_0|/\tau_{\text{dec}}) \right), \quad (\text{S21})$$

where c is a global normalization factor.

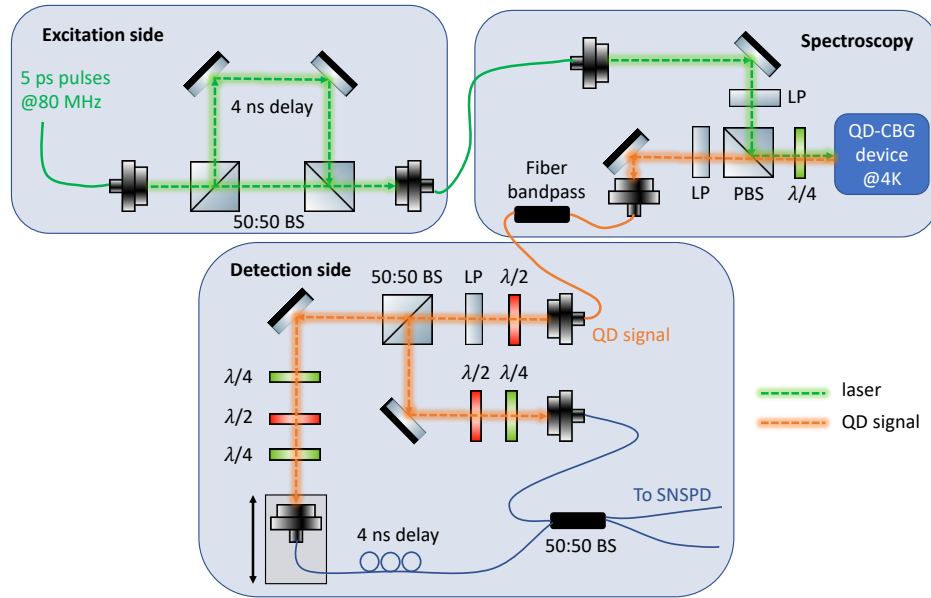
The extracted fit parameters for the quasi-resonantly excited autocorrelation data shown in the main text and in Supplementary Figs. S14b-S14c are shown in Supplementary Tab. S6. Note that in real applications temporal filtering is not always possible which is why we state also the integrated value. For that, we integrate all coincidences in a window of ± 6 ns around each peak in the histogram. Then, we divide the sum of coincidences in the center window by the average of the sums in all side windows, as no blinking is present. The uncertainty is based on the variance of integrated side peak areas.

Supplementary Table S6. Fitting parameters for quasi-resonant autocorrelation measurement.

Fit parameter	Quasi-resonant excitation power		
	$P_{\text{exc}} = 0.6 \mu\text{W}$ ($0.02 \times P_{\text{sat}}$), Fig. S14b	$P_{\text{exc}} = 1.5 \mu\text{W}$ ($0.04 \times P_{\text{sat}}$), Fig. 4a	$P_{\text{exc}} = 40 \mu\text{W}$ (P_{sat}), Fig. S14c
Decay time, τ_{dec}	$(606 \pm 3) \text{ ps}$	$(584 \pm 3) \text{ ps}$	$(591 \pm 7) \text{ ps}$
Laser period, τ_0	$(12.49 \pm 0.01) \text{ ns}$	$(12.49 \pm 0.01) \text{ ns}$	$(12.49 \pm 0.01) \text{ ns}$
$g^{(2)}(0)_{\text{fit}}$	$(5.6 \pm 5.0) \times 10^{-3}$	$(4.7 \pm 2.6) \times 10^{-3}$	$(9.81 \pm 1.94) \times 10^{-2}$
$g^{(2)}(0)_{\text{raw}}$	$(4.2 \pm 0.2) \times 10^{-3}$	$(3.2 \pm 0.6) \times 10^{-3}$	$(8.75 \pm 4.88) \times 10^{-2}$

D. Indistinguishability measurements and data analysis

Supplementary Fig. S15 presents the configuration of the experimental setup applied to record the HOM histograms. The 4 ns excitation delay is compensated on the detection side. A cross-polarization setup suppresses the reflected laser light and a 0.4 nm fiber bandpass spectrally filters the emission. The HOM setup consists of a 50:50 free-space beam splitter and a 50:50 fiber beam splitter in which the interference takes place. The fiber in-coupling can be translated for optimization of the temporal matching and the polarization is set in free space via waveplates and confirmed with a polarimeter.



Supplementary Fig. S15. The HOM experimental setup. BS – beam splitter, $\lambda/2$, $\lambda/4$ – half and quarter wave-plate, SNSPD – superconducting nanowire single-photon detector.

The indistinguishability measurements were performed with a 4 ns delay. To do so, the train of laser pulses arriving every 12.5 ns was split on the excitation side into two pulses separated by a delay of 4 ns which was compensated on the detection side, to interfere subsequently emitted photons in a fiber beam splitter. The laser was tuned to excite the QD-CBG quasi-resonantly for three excitation powers, $P_{\text{exc}} = 0.6 \mu\text{W}$ ($0.02 \times P_{\text{sat}}$), $P_{\text{exc}} = 1.5 \mu\text{W}$ ($0.04 \times P_{\text{sat}}$), and $P_{\text{exc}} = 40 \mu\text{W}$ (P_{sat}).

The obtained histograms are composed of a characteristic pattern of 5 peaks repeated every 12.5 ns corresponding to the 80 MHz repetition rate of the excitation laser. They are related to coincidences resulting from consecutive photons taking different paths in the imbalanced Mach-Zehnder interferometer (MZI). There are 5 possible final delay combinations leading to the observed pattern [19]. For the Poissonian statistics of the emission, the intensity ratio of the 5 non-central peaks is expected to be 1:4:6:4:1, whereas for the center peak (produced by coincidences originating in the pair of laser pulses separated by 4 ns), indistinguishable single photons produce the combination of coincidences 1:2:0:2:1 in contrast to 1:2:2:2:1 for completely distinguishable photons.

The figure of merit for the photon indistinguishability can be extracted from HOM measurements in different ways. Typically, the amount of coincidences in the case of expected indistinguishability is compared to the number of coincidences for expected maximum distinguishability, either at cross-polarized interference or from different laser pulses (photons that have not interfered). As the second approach with side peaks is more susceptible to blinking and imperfect setups, we determine the indistinguishability from the comparison of co- and cross-polarized HOM measurements and extract the visibility as the ratio of the central peak areas via

$$V = 1 - A_{\text{Co}}/A_{\text{Cross}}, \quad (\text{S22})$$

while we still mention the values obtained from the side peak method for completeness at the end of this section. In order to extract also other physical quantities and to compensate for statistical fluctuations the data is fitted according to the model described below and the areas $A_{\text{Co}} = A_3$ for the co-polarized case and $A_{\text{Cross}} = A_3$ for the cross-polarized case are obtained.

To properly fit the entire HOM coincidence histograms one has to keep in mind that the areas of the ± 4 ns side peaks belonging to a laser pulse at the time delay $\tau = 0$ ns already overlap with the areas from the side peaks originating from the ± 8 ns laser excitation at $\tau = \pm 12.5$ ns (as they are present in the histogram at ± 4.5 ns), see Supplementary Fig. S16. Consequently, the individual contributions can be extracted by fitting the data by the sum of all contributions according to the formula. For the HOM histogram recorded for the co-polarized case, the formula reads

$$C_{\text{HOM,Co}}(\tau, [\tau_1, T_2, \Delta t, \tau_0, \mathbf{A}, \mathbf{B}]) = A_3 \exp(-|\tau|/\tau_1) \left(1 - V_{\text{PS}} \cdot e^{-|\tau|/T_2} \right) + \sum_{i=\{1,2,4,5\}} A_i \exp(-|\tau + \Delta t_i|/\tau_1) \quad (\text{S23})$$

$$+ \sum_{n=-10, n \neq 0}^{10} \left[\sum_{i=\{1,2,3,4,5\}} B_i \exp(-|\tau + \Delta t_i + n \cdot \tau_0|/\tau_1) \right],$$

and for the cross-polarized data

$$C_{\text{HOM,Cross}}(\tau, [\tau_1, T_2, \Delta t, \tau_0, \mathbf{A}, \mathbf{B}]) = A_3 \exp(-|\tau|/\tau_1) + \sum_{i=\{1,2,4,5\}} A_i \exp(-|\tau + \Delta t_i|/\tau_1) \quad (\text{S24})$$

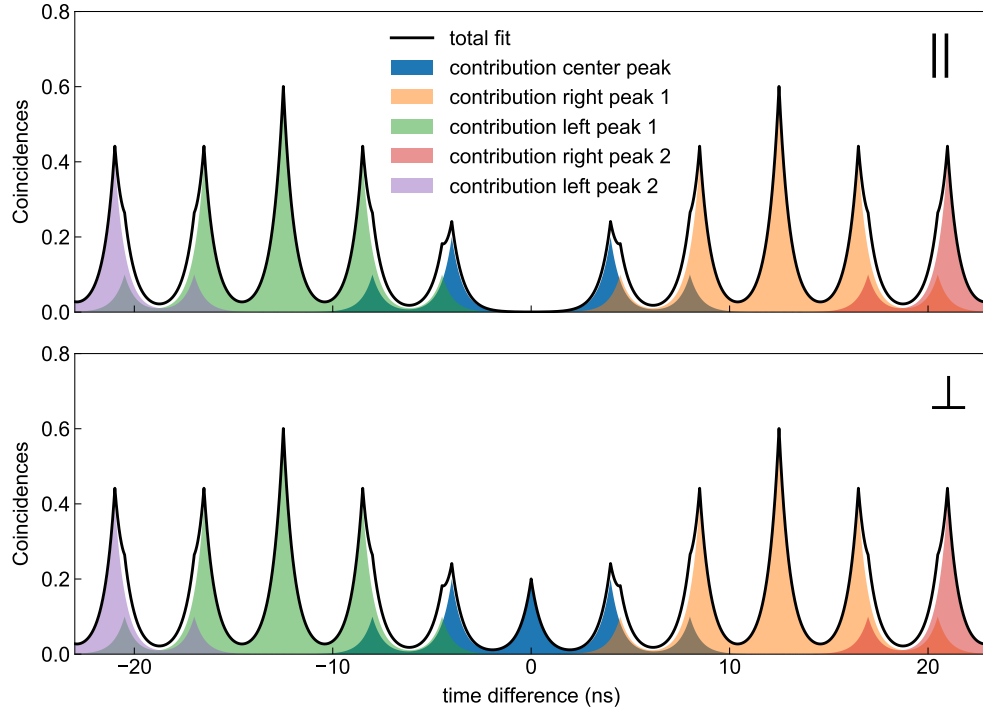
$$+ \sum_{n=-10, n \neq 0}^{10} \left[\sum_{i=\{1,2,3,4,5\}} B_i \exp(-|\tau + \Delta t_i + n \cdot \tau_0|/\tau_1) \right].$$

These formulas for the normalized coincidences as a function of the detection time difference τ includes the 4 ns delay between two interfering photons $\Delta t_{1-5} = \{-8, -4, 0, 4, 8\}$ ns, the 12.5 ns initial laser pulse delay τ_0 , the photoluminescence decay time τ_1 , the coherence time T_2 , the post-selected visibility V_{PS} , the respective peak heights of the center 5-peak-structure A_{1-5} , and the averaged peak heights of all peaks at higher delays B_{1-5} . The two fits for co- and cross-polarized cases differ only by the existence of the volcano-shaped dip in the central peak of the co-polarized data, being the fingerprint of the two-photon interference. The post-selected visibility is the value one obtains also when comparing the center peak contribution of the co- and the cross-case at $\tau = 0$ as then

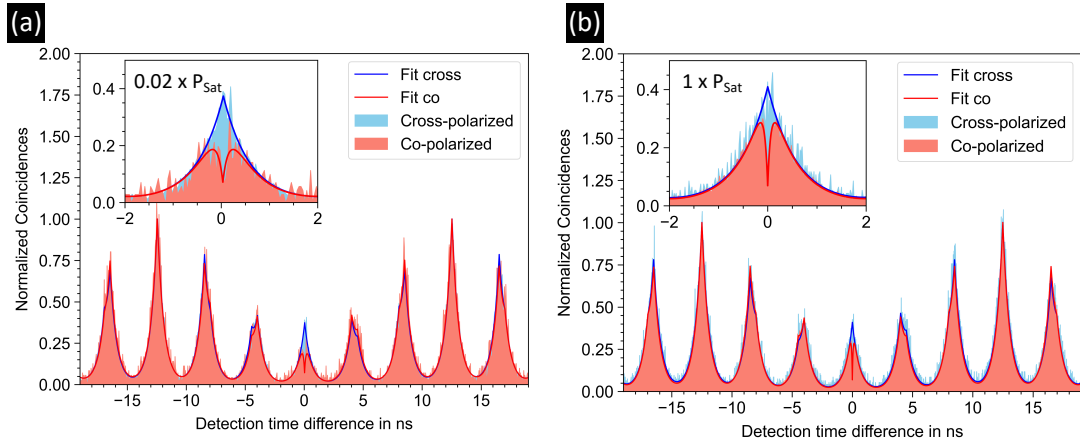
$$V_{\text{PS}} = 1 - \frac{C_{\text{HOM,Co}}(\tau = 0)}{C_{\text{HOM,Cross}}(\tau = 0)} = 1 - \frac{A_3(1 - V_{\text{PS}})}{A_3}. \quad (\text{S25})$$

The simulated histograms for our experimental parameters expected from this model are shown in Supplementary Fig. S16 top and bottom for perfectly indistinguishable and distinguishable photons, respectively.

While the fitted histogram for $0.04 \times P_{\text{sat}}$ is presented in the article, Fig. 4b, the fitted histograms for $0.02 \times P_{\text{sat}}$ and P_{sat} excitation powers are shown in Supplementary Fig. S17 and the extracted parameters in Supplementary Tab. S7. All fits were done on the unbinned raw data without correcting for finite $g^{(2)}(0)$, as the obtained $g^{(2)}(0)$ values are small. Additionally, the fits do not include corrections for the detector time response or subtracting a fixed background. The uncertainties are determined from the fit errors and propagated whenever a quantity was calculated from the fit parameters.



Supplementary Fig. S16. Expected HOM histograms of coincidences with individual peak contributions to the five peak patterns formed by 4 ns delay and laser repetition of $\tau_0 = 12.5$ ns, **a**, for perfectly indistinguishable photons, and **b**, for maximally distinguishable photons. The black lines represent the fits according to Eqs. (S23)–(S24) that include all contributions, plotted for $\tau_1 = 550$ ps lifetime.



Supplementary Fig. S17. Comparison of HOM histograms taken at **a**, $0.02 \times P_{\text{sat}}$ and **b**, P_{sat} excitation power. HOM measurement recorded for $0.02 \times P_{\text{sat}}$ shows higher indistinguishability and longer coherence time than the one taken at P_{sat} , see Supplementary Tab. S7.

One can clearly see from the graph that the photon indistinguishability is reduced at higher power, as evidenced by the larger central peak area. That is confirmed also by the extracted visibilities of $(22.1 \pm 8.9)\%$, $(19.3 \pm 2.6)\%$ and $(11.3 \pm 2.3)\%$ for low to high power. That is partly due to a worse single-photon purity at P_{sat} (see Supplementary Fig. S14c) but mainly due to a reduced coherence, as indicated by the narrower central dip at higher excitation power. We find that the coherence time T_2 is reduced from (176 ± 9) ps over (103 ± 13) ps to (74 ± 6) ps with the increasing excitation power. The extracted post-selected values are $V_{\text{ps}} = (80 \pm 13)\%$, $(99 \pm 6)\%$ and $(84 \pm 3)\%$ without clear dependence on the excitation power within the determined

Supplementary Table S7. Extracted fitting parameters for recorded HOM histograms. MFR – mean fit residuals.

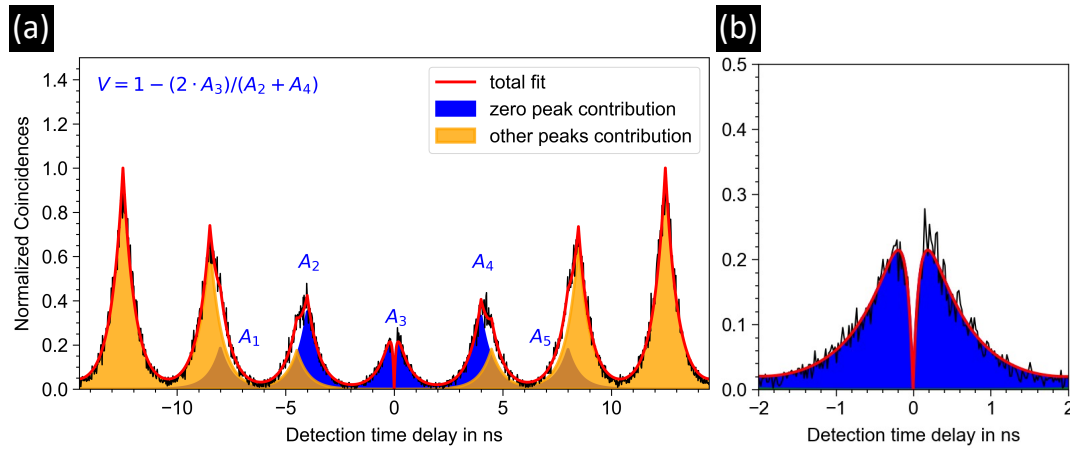
Fit parameter	Quasi-resonant excitation power					
	$0.02 \times P_{\text{sat}}$, shown in Fig. S17a		$0.04 \times P_{\text{sat}}$, shown in Fig. 4b		P_{sat} , shown in Fig. S17b	
Co-pol areas A, B	$\begin{pmatrix} 1.00 \pm 0.11 \\ 2.08 \pm 0.11 \\ 1.77 \pm 0.21 \\ 2.14 \pm 0.11 \\ 1.38 \pm 0.11 \end{pmatrix}$	$\begin{pmatrix} 1.00 \pm 0.06 \\ 4.23 \pm 0.05 \\ 6.66 \pm 0.04 \\ 4.55 \pm 0.05 \\ 1.27 \pm 0.06 \end{pmatrix}$	$\begin{pmatrix} 1.00 \pm 0.04 \\ 1.84 \pm 0.04 \\ 1.68 \pm 0.05 \\ 1.95 \pm 0.04 \\ 1.03 \pm 0.04 \end{pmatrix}$	$\begin{pmatrix} 1.00 \pm 0.02 \\ 3.76 \pm 0.02 \\ 5.69 \pm 0.02 \\ 3.75 \pm 0.02 \\ 1.03 \pm 0.02 \end{pmatrix}$	$\begin{pmatrix} 1.00 \pm 0.02 \\ 1.96 \pm 0.02 \\ 2.02 \pm 0.03 \\ 1.92 \pm 0.02 \\ 0.95 \pm 0.02 \end{pmatrix}$	$\begin{pmatrix} 1.00 \pm 0.01 \\ 3.78 \pm 0.01 \\ 5.68 \pm 0.01 \\ 3.75 \pm 0.01 \\ 0.98 \pm 0.01 \end{pmatrix}$
Cross-pol area A_3 ,	2.28 ± 0.04		2.08 ± 0.04		2.27 ± 0.06	
Lifetime, τ_1	(559 ± 4) ps		(553 ± 2) ps		(563 ± 7) ps	
Coherence time, T_2	(176 ± 9) ps		(103 ± 13) ps		(74 ± 6) ps	
V_{ps}	(80 ± 13) %		(99 ± 6) %		(84 ± 3) %	
MFR, Co fit	0.0812		0.0286		0.0158	
MFR, Cross fit	0.0280		0.0280		0.0526	
TPI visibility, V	(22.1 ± 8.9) %		(19.3 ± 2.6) %		(11.3 ± 2.3) %	

fit uncertainty and mainly limited by the detector timing resolution. The larger uncertainties for the fit parameters for the HOM histogram recorded at $0.02 \times P_{\text{sat}}$ are caused by the lower gathered statistics as indicated also by the larger mean fit residuals (MFR) for the fit of the co-polarized case (0.0812 vs. 0.0280). Note that for the same reason, the deviation from the expected peak ratios is larger in this case as well. The remaining deviations from the expected 5-peak-ratios (**A, B**) can also be caused by unequal transmissions in the two arms of the MZIs.

As mentioned at the beginning of this section, in addition to comparing the areas of the co- and cross-polarized central peak, the indistinguishability can also be extracted by comparing the areas of the central to the outer peaks for only the co-polarized data. This analysis of the low-power HOM histogram is presented in Supplementary Fig. S18. Evaluating the visibility from the extracted center A_3 and side peak areas A_2, A_4 , and calculating the visibility as $V_{\text{side peaks}} = 1 - 2A_3/(A_2 + A_4)$ leads to (15.9 ± 9.9) % for the low excitation power ($0.02 \times P_{\text{sat}}$), which agrees with the visibility result reported above obtained from the co-cross-comparison. The uncertainty is however larger, as the fitting relies on successfully separating the overlapping peak contributions.

Importantly, the obtained visibilities and the post-selected values compare favorably with the reports for GaAs-based QDs emitting at C-band [20–22]. For planar QDs, a visibility of (14.4 ± 1.5) % has been reported under pulsed resonant excitation [21] while the raw visibility value of (71 ± 15) % was obtained under two-photon-resonant cw excitation [20]. Values obtained under cw excitation can be related to the post-selected values determined from pulsed excitation. For QDs placed non-deterministically in CBGs, the only reported visibility so far is (8.1 ± 3.4) % and the post-selected on the order of 60 % [22].

-
- [1] U. M. Gür, S. Arslanagić, M. Mattes, and N. Gregersen, Open-geometry modal method based on transverse electric and transverse magnetic mode expansion for orthogonal curvilinear coordinates, *Phys. Rev. E* **103**, 033301 (2021).
 - [2] L. Novotny and B. Hecht, *Principles of Nano-Optics*, 2nd ed. (Cambridge University Press, 2012).
 - [3] A. V. Lavrinenko, J. Lægsgaard, and N. Gregersen, *Numerical Methods in Photonics* (CRC PR INC, 2014).
 - [4] L. Li, Formulation and comparison of two recursive matrix algorithms for modeling layered diffraction gratings, *J. Opt. Soc. Amer. A* **13**, 1024 (1996).
 - [5] C. A. Balanis, *Antenna Theory: Analysis and Design* (Wiley John + Sons, 2016).
 - [6] B. Yao, R. Su, Y. Wei, Z. Liu, T. Zhao, and J. Liu, Design for Hybrid Circular Bragg Gratings for a Highly Efficient Quantum-Dot Single-Photon Source, *J. Korean Phys. Soc.* **73**, 1502 (2018).
 - [7] P. Holewa, A. Sakanas, U. M. Gür, P. Mrowiński, A. Huck, B.-Y. Wang, A. Musiał, K. Yvind, N. Gregersen, M. Syperek, and E. Semenova, Bright Quantum Dot Single-Photon Emitters at Telecom Bands Heterogeneously Integrated on Si, *ACS Photonics* **9**, 2273 (2022).
 - [8] A. Sakanas, E. Semenova, L. Ottaviano, J. Mørk, and K. Yvind, Comparison of processing-induced deformations of InP bonded to Si determined by e-beam metrology: Direct vs. adhesive bonding, *Microelectron. Eng.* **214**, 93 (2019).
 - [9] B. Zhang, J. Zerubia, and J.-C. Olivo-Marin, Gaussian approximations of fluorescence microscope point-spread function models, *Appl. Opt.* **46**, 1819 (2007).
 - [10] J. Liu, M. I. Davanço, L. Sapienza, K. Konthasinghe, J. V. D. M. Cardoso, J. D. Song, A. Badolato, and K. Srinivasan, Cryogenic photoluminescence imaging system for nanoscale positioning of single quantum emitters, *Rev. Sci. Instrum.* **88**, 023116 (2017).



Supplementary Fig. S18. Data analysis of the low-power HOM histogram. **a**, Individual peak contributions extracted as part of the total fit according to Eq. (S23) for the lowest power HOM measurement ($0.02 \times P_{\text{sat}}$). **b**, Close-up of the central peak.

- [11] J. D. Lambkin, D. J. Dunstan, K. P. Homewood, L. K. Howard, and M. T. Emeny, Thermal quenching of the photoluminescence of InGaAs/GaAs and InGaAs/AlGaAs strained-layer quantum wells, *Appl. Phys. Lett.* **57**, 1986 (1990).
- [12] P. Holewa, M. Gawelczyk, C. Ciostek, P. Wyborski, S. Kadkhodazadeh, E. Semenova, and M. Sypersek, Optical and electronic properties of low-density InAs/InP quantum-dot-like structures designed for single-photon emitters at telecom wavelengths, *Phys. Rev. B* **101**, 195304 (2020).
- [13] C. Santori, M. Pelton, G. Solomon, Y. Dale, and Y. Yamamoto, Triggered single photons from a quantum dot, *Phys. Rev. Lett.* **86**, 1502 (2001).
- [14] M.-E. Pistol, P. Castrillo, D. Hessman, J. A. Prieto, and L. Samuelson, Random telegraph noise in photoluminescence from individual self-assembled quantum dots, *Phys. Rev. B* **59**, 10725 (1999).
- [15] H. Robinson and B. Goldberg, Light-induced spectral diffusion in single self-assembled quantum dots, *Phys. Rev. B* **61**, R5086 (2000).
- [16] P. A. Dalgarno, J. McFarlane, D. Brunner, R. W. Lambert, B. D. Gerardot, R. J. Warburton, K. Karrai, A. Badolato, and P. M. Petroff, Hole recapture limited single photon generation from a single n-type charge-tunable quantum dot, *Appl. Phys. Lett.* **92**, 193103 (2008).
- [17] T. Miyazawa, K. Takemoto, Y. Nambu, S. Miki, T. Yamashita, H. Terai, M. Fujiwara, M. Sasaki, Y. Sakuma, M. Takatsu, T. Yamamoto, and Y. Arakawa, Single-photon emission at 1.5 μm from an InAs/InP quantum dot with highly suppressed multi-photon emission probabilities, *Appl. Phys. Lett.* **109**, 132106 (2016).
- [18] G. Irmer, M. Wenzel, and J. Monecke, The temperature dependence of the LO(T) and TO(T) phonons in GaAs and InP, *Phys. Status Solidi B* **195**, 85 (1996).
- [19] A. Thoma, P. Schnauber, M. Gschrey, M. Seifried, J. Wolters, J. H. Schulze, A. Strittmatter, S. Rodt, A. Carmele, A. Knorr, T. Heindel, and S. Reitzenstein, Exploring dephasing of a solid-state quantum emitter via time- and temperature-dependent Hong-Ou-Mandel experiments, *Phys. Rev. Lett.* **116**, 1 (2016).
- [20] C. Nawrath, F. Olbrich, M. Paul, S. L. Portalupi, M. Jetter, and P. Michler, Coherence and indistinguishability of highly pure single photons from non-resonantly and resonantly excited telecom C-band quantum dots, *Appl. Phys. Lett.* **115**, 023103 (2019).
- [21] C. Nawrath, H. Vural, J. Fischer, R. Schaber, S. L. Portalupi, M. Jetter, and P. Michler, Resonance fluorescence of single In(Ga)As quantum dots emitting in the telecom C-band, *Appl. Phys. Lett.* **118**, 244002 (2021).
- [22] C. Nawrath, R. Joos, S. Kolatschek, S. Bauer, P. Pruy, F. Hornung, J. Fischer, J. Huang, P. Vijayan, R. Sittig, M. Jetter, S. L. Portalupi, and P. Michler, High emission rate from a Purcell-enhanced, triggered source of pure single photons in the telecom C-band, *arXiv:2207.12898 [quant-ph]* (2022).